

EVALUATION AND SELECTION OF SST REGRESSION ALGORITHMS FOR JPSS VIIRS

Boris Petrenko^{1,2}, Alexander Ignatov¹, Yury Kihai^{1,2}, John Stroup^{1,3}, Prasanjit Dash^{1,4}

¹NOAA Satellite and Information Service, Center for Satellite Applications and Research (STAR),
College Park, Maryland, USA

²GST, Inc., Greenbelt, Maryland, USA

³STG, Inc., Reston, Virginia, USA

⁴CIRA, Fort Collins, Colorado, USA

Corresponding author: B. Petrenko, NCWCP, Rm 3724, 5830 University Research Court, College
Park, MD 20704, USA (e-mail: boris.petrenko@noaa.gov, Tel.: 1-301-683-3359)

Key points

- Regression SST algorithms for VIIRS are selected from existing SST algorithms
- Algorithm metric is defined as area in which SST specifications are met
- Selected algorithms emphasize angular dependencies of regression coefficients

Index terms

Instruments and techniques, Ocean observing systems

Keywords

Sea surface temperature, algorithm, regression, accuracy, precision, sensitivity

ABSTRACT

Two global Level 2 SST products are generated at NOAA from the SNPP VIIRS sensor data records (L1) with two independent processing systems, the Joint Polar Satellite System (JPSS) Interface Data Processing Segment (IDPS), and the NOAA heritage Advanced Clear Sky Processor for Oceans (ACSPO). The two systems use different SST retrieval and cloud masking algorithms. Validation against in situ and L4 analyses has shown suboptimal performance of the IDPS product. In this context, existing operational and proposed SST algorithms have been evaluated for their potential implementation in IDPS. This paper documents the evaluation methodology and results. The performance of SST retrievals is characterized with bias and standard deviation with respect to in situ SSTs, and sensitivity to true SST. Given three retrieval metrics, all being variable in space and with observational conditions, an additional integral metric is needed to evaluate the overall performance of SST algorithms. Therefore, we introduce the Quality Retrieval Domain (QRD) as a part of the global ocean, where the retrieval characteristics meet predefined specifications. Based on the QRDs analyses for all tested algorithms over a representative range of specifications for accuracy, precision, and sensitivity, we have selected the algorithms developed at the EUMETSAT Ocean and Sea Ice Satellite Application Facility (OSI-SAF) for implementation in IDPS and ACSPO. Testing the OSI-SAF algorithms with ACSPO and IDPS products shows the improved consistency between VIIRS SST and Reynolds L4 daily analysis. Further improvement of the IDPS SST product requires adjustment of the VIIRS Cloud and Ice Masks.

INTRODUCTION

The Visible Infrared Imaging Radiometer Suite (VIIRS; see Table 1 for list of abbreviations used in the paper) has been flown onboard the Suomi National Polar-orbiting Partnership (SNPP) satellite since 28 October 2011. The VIIRS will also be onboard the two follow-on Joint Polar Satellite System (JPSS) satellites, J1 and J2, scheduled for launch in 2017 and 2023, respectively.

Sea surface temperature (SST, T_s) is one of the key global JPSS products. The algorithms and software for SST retrieval from VIIRS were developed for the former National Polar-orbiting Environmental Satellite System (NPOESS) by a private contractor, Northrop Grumman Aerospace Systems [NGAS; *Jackson and Siebels, 2011*], and operationally implemented within the Interface Data Processing Segment (IDPS) system that is run by another NPOESS contractor, Raytheon. In 2011, the NPOESS Program underwent restructuring and transformed into the Joint Polar Satellite System (JPSS) Program, managed by the National Oceanic and Atmospheric Administration (NOAA). Today, the NOAA Center for Satellite Applications and Research (STAR) is responsible for the JPSS algorithms and calibration/validation (Cal/Val) activities, while Raytheon continues operating the IDPS system.

During the NPOESS era, all major centers producing L2 SST products, including NOAA, Naval Oceanographic Office (NAVO), University of Miami, and EUMETSAT Ocean and Sea Ice Satellite Application Facility (OSI-SAF) continued development and adaptation of their heritage SST systems to process VIIRS data. This was deemed important to ensure continuity for operational users. Also, some NPOESS algorithms were viewed as risky by operational agencies. In particular, NOAA funded the effort to adapt its heritage Advanced Clear-Sky Processor for Oceans system (ACSPO;

[Ignatov et al., 2011, 2012]), under the NOAA Data Exploitation (NDE) program. The operational production of ACSPO SST within NDE is expected to commence in February 2014. In the meantime, STAR started generating an experimental ACSPO SST product from VIIRS data on 21 January 2012, simultaneously with the IDPS system, after the VIIRS thermal regime stabilized following the opening of its cryoradiator doors on 18 January 2012. Since that date, IDPS and ACSPO SST products, generated by Raytheon and STAR, respectively, have been continuously monitored in the NOAA SST Quality Monitor [SQUAM, www.star.nesdis.noaa.gov/sod/sst/squam/; Dash et al., 2010]. Also, clear-sky brightness temperatures in VIIRS bands M12, M15, and M16, centered at 3.7, 11, and 12 μm , respectively, and currently used for SST retrievals, have been monitored in the Monitoring of IR Clear-sky Radiances over Oceans for SST [MICROS; www.star.nesdis.noaa.gov/sod/sst/micros/; Liang and Ignatov, 2011, 2013].

Validation of IDPS and ACSPO SST products against in situ SST, T_S^i , and comparisons with Level 4 analyses, such as AVHRR-based 0.25° Daily High-Resolution-Blended SST analysis (DSST) [Reynolds et al., 2007] and Operational SST and Sea Ice Analysis (OSTIA) [Donlon et al., 2012] in SQUAM, have shown that the performance of the IDPS SST is suboptimal compared to ACSPO. This has prompted the need for more efficient SST algorithms for VIIRS. This paper documents methodology and results of these analyses.

Note that this study was undertaken under serious time and funding constraints, during the transition from NPOESS to JPSS, and therefore only explores well tested heritage approaches adopted in the major SST centers around the world. Currently, all existing operational systems (including IDPS) retrieve SST from observed brightness temperatures (BT, T_B) via regression, using

modifications of two approaches developed for the Advanced Very High Resolution Radiometer (AVHRR) onboard NOAA and MetOp satellites. The “Multichannel” SST (MCSST) [McClain et al., 1985] is customarily used with three bands centered at 3.7, 11, and 12 μm , at night only. During daytime, the 3.7 μm band is affected by reflected solar radiance and therefore not used. The “Nonlinear” SST (NLSST) [Walton et al., 1998] customarily exploits two split-window bands centered at 11 and 12 μm and a priori SST, T_s^0 , which is used as a proxy for atmospheric humidity. Although the NLSST is mostly used during daytime, it can be also used at night, in conjunction with the more transparent 3.7 μm band. As shown in Section 2 below, all operational centers use different implementations of the SST equations, which need to be cross-evaluated and reconciled. Analyses of “AVHRR-like” algorithms for VIIRS in this study, allows placing JPSS algorithms in context of other existing operational SST systems, and using them as a benchmark for future improvements.

Enhancements based on using more generic forms of SST regression equations (e.g., Llewellyn-Jones et al., 1984) are being explored for the J1 VIIRS to be launched in 2017. Considering the need for quick “common sense” fixes in the IDPS system, we have opted to only include well tested operational algorithms in the present analyses. Exploring potential of optional VIIRS bands M13 and M14 (centered at 4.05 and 8.55 μm) is also underway..

Physical retrievals based on radiative transfer model (RTM) simulations also continue to be investigated in the SST community [e.g., Merchant et al, 2009a; Le Borgne et al., 2011; Petrenko et al., 2011], and will be considered for the J1 VIIRS depending upon their advance and readiness. Currently, some operational systems (e.g., ACSPO and OSI SAF) support RTM simulations and RTM-based SST retrievals, but only in an experimental mode. The current implementation of the

IDPS system does not support RTM simulations in VIIRS SST bands. All radiative transfer simulations used in this study have been performed using ACSPO, which incorporates the Community Radiative Transfer Model (CRTM) in conjunction with first guess SST and atmospheric profiles fields [Liang et al., 2009; Liang and Ignatov, 2011, 2013].

The paper is structured as follows. Evaluated SST algorithms are discussed in Section 2. Section 3 explains the selection of metrics for algorithms evaluation and comparison. Section 4 describes the methodology of calculations for these metrics. Sections 5 and 6 present results of the evaluation of daytime and nighttime algorithms, respectively. Section 7 discusses results of implementation and testing of SST algorithms against L4 SST (DSST) within IDPS and ACSPO. Section 8 summarizes and concludes.

2 TESTED SST ALGORITHMS

2.1 ACSPO

ACSPO is a processing system developed at NOAA STAR. Since May 2008, ACSPO has been used for operational processing of the AVHRR data at the NOAA Office of Satellite and Product Operations (OSPO). The newer ACSPO versions are being continuously developed and used at STAR for experimental processing of data from all AVHRR, Moderate Resolution Imaging Spectroradiometer (MODIS), and VIIRS sensors [Ignatov et al., 2012; Liang and Ignatov, 2013]. As of this writing, ACSPO employs heritage regression SST equations implemented earlier in the ACSPO predecessor, the NOAA Main Unit Task system [Ignatov, 2004]. However, the coefficients of regression equations were recalculated to accommodate the new ACSPO clear-sky mask

[Petrenko et al., 2010], and to extend retrievals to full sensors' swaths. At night (i.e., solar zenith angle, $\text{SZA} > 90^\circ$), the ACSPO uses an MCSST equation of the following form:

$$T_S = a_0 + a_1 T_{B11} + a_2 T_{B3.7} + a_3 T_{B12} + a_4 \Delta T_{3.7-12} S_\theta + a_5 S_\theta. \quad (1)$$

The daytime ACSPO equation is of NLSST type:

$$T_S = b_0 + b_1 T_{B11} + b_2 \Delta T_{11-12} (T_S^0 + X) + b_3 \Delta T_{11-12} S_\theta. \quad (2)$$

Here, $T_{B3.7}$, T_{B11} , and T_{B12} are BTs at 3.7 μm (AVHRR channel 3B, MODIS band 20, and VIIRS band M12), 11 μm (Ch4, band 31 and M15), and 12 μm (Ch5, band 32, and M16), respectively; T_S^0 is a first guess SST (in kelvin) obtained from the analysis (L4) SST field, such as the DSST; $\Delta T_{3.7-12} = T_{B3.7} - T_{B12}$; $\Delta T_{11-12} = T_{B11} - T_{B12}$; $X = -273.15$ is an offset, which transforms T_S^0 into degrees Celsius; $S_\theta = \sec\theta - 1$; and a_i ($i=0,1\dots5$) and b_i ($i=0,1,2,3$) are regression coefficients.

2.2 Pathfinder and NASA MODIS algorithms

Pathfinder (PF) SST is produced at the NOAA National Oceanographic Data Center (NODC) from AVHRR data using the same NLSST algorithm defined by Eq. (2) for day and night, but with two separate sets of coefficients for “low” and “high” atmospheric humidity. The wet/dry conditions are identified by the value of ΔT_{11-12} as follows [Kilpatrick et al., 2001; Evans and Podesta, 1998; Casey et al., 2010]:

$$T_S = T_S^L, \text{ if } \Delta T_{11-12} < \Delta T_{11-12}^L; \quad (3a)$$

$$T_S = T_S^H, \text{ if } \Delta T_{11-12} > \Delta T_{11-12}^H; \quad (3b)$$

$$T_S^L = a_0^L + a_1^L T_{B11} + a_2^L \Delta T_{11-12} (T_S^0 + X) + a_3^L \Delta T_{11-12} S_\theta; \quad (3c)$$

$$T_S^H = a_0^H + a_1^H T_{B11} + a_2^H \Delta T_{11-12} (T_S^0 + X) + a_3^H \Delta T_{11-12} S_\theta. \quad (3d)$$

For intermediate ΔT_{11-12} values, $\Delta T_{11-12}^L \leq \Delta T_{11-12} \leq \Delta T_{11-12}^H$, T_S is found by interpolation:

$$T_S = T_S^L + (T_S^H - T_S^L) (\Delta T_{11-12} - \Delta T_{11-12}^L) / (\Delta T_{11-12}^H - \Delta T_{11-12}^L). \quad (3e)$$

Here, $X = -273.15$ K (first guess SST in Celsius), $\Delta T_{11-12}^L = 0.5$ K, and $\Delta T_{11-12}^H = 0.9$ K.

Regression coefficients for low humidity conditions, a_i^L are derived from the part of matchups with $\Delta T_{11-12} < (\Delta T_{11-12}^H + \Delta T_{11-12}^L)/2$, and the coefficients for high humidity conditions, a_i^H are derived from matchups with $\Delta T_{11-12} > (\Delta T_{11-12}^H + \Delta T_{11-12}^L)/2$.

The NASA MODIS algorithm employed to generate the MO(Y)D28 product is the PF wet/dry NLSST, except at night, “shortwave” SST4 is additionally generated from MODIS bands 21 (centered at 3.9 μm) and 22 (4.0 μm) [Brown and Minnett, 1999; Minnett et al., 2004; Franz, 2006]. SST4 is included in the M*D28 data set, and used as T_S^0 in Eq. (2). The band 21 centered at 3.9 μm is not available on VIIRS. Therefore, in this study, the nighttime MODIS SST4 algorithm was not considered, and DSST was used as the first-guess SST on the right side of Eq. (2) instead of SST4.

As of this writing, the wet/dry stratified NLSST algorithm has been employed in all PF versions up to v5.2, and all M*D28 production including collection 5. The plan is to transition in PF v6 and M*D28 collection 6 to the LATBAND algorithm described in section 2.4 below [R. Evans, 2013, personal communication].

2.3 IDPS

In the JPSS IDPS system, the daytime SST algorithm is similar to that of Pathfinder (3, a-e), but with $\Delta T_{11-12}^L = 0.6$ K and $\Delta T_{11-12}^H = 1$ K [Jackson and Siebels, 2011]. Furthermore, X is set to 0 K,

163 meaning that T_s^0 is used in kelvin rather than degrees Celsius. The nighttime IDPS algorithm uses
 164 the following equation, in which T_s^0 is also in kelvin:

$$165 \quad T_S = a_0 + a_1 T_{B11} + a_2 \Delta T_{3.7-12} T_s^0 + a_3 S_\theta. \quad (4)$$

166 2.4 LATBAND

167 The LATBAND algorithm was proposed to minimize geographical biases [Minnett and Evans,
 168 2009]. The LATBAND SST and SST4 equations have the same form as the wet/dry NLSST
 169 formulations employed in PF v5 and M*D28 collection 5 as described in section 2.2, but with
 170 coefficients separately calculated for 6 zonal bands: $\lambda \leq -40^\circ$, $-40^\circ < \lambda \leq -20^\circ$, $-20^\circ < \lambda \leq 0^\circ$, $0^\circ < \lambda$
 171 $\leq 20^\circ$, $20^\circ < \lambda \leq 40^\circ$, $\lambda \geq 40^\circ$ and for each month of the year. Transitions between separate zonal
 172 bands are processed with a smoothing interpolation algorithm.

173 2.5 OSI-SAF

174 The SST algorithms developed at OSI-SAF employ modifications of NLSST and MCSST in
 175 which dependencies of regression coefficients on view zenith angle (VZA) are emphasized [Brisson
 176 et al., 2002; OSI-SAF Low Earth Orbiter SST Product User Manual, 2009]. Here, we will use the
 177 formulations of the OSI-SAF equations suggested specifically for VIIRS by Lavanant et al. [2012].
 178 The daytime equation is the analogue of equation (2), in which the coefficients in front of all
 179 regressors are more complete functions of S_θ . Also, note that the X in the OSI-SAF NLSST
 180 algorithm is set to -273.15 K (first guess SST is expressed in Celsius):

$$181 \quad T_S = b_0 + (b_1 + b_2 S_\theta) T_{11} + [b_3 + b_4 (T_s^0 + X) + b_5 S_\theta] \Delta T_{11-12} + b_6 S_\theta. \quad (5)$$

182 The dependencies of coefficients on S_θ are also more complete in the nighttime equation:

$$T_s = a_0 + (a_1 + a_2 S_\theta) T_{3.7} + (a_3 + a_4 S_\theta) \Delta T_{11-12} + a_5 S_\theta. \quad (6)$$

2.6 NAVO

All NLSST algorithms mentioned above use T_s^0 either in degrees Celsius ($X=-273.15$) or in kelvin ($X=0$). Cayula et al. [2013] of NAVO suggested deriving the optimal X value for the daytime equation from matchups along with other regression coefficients, leading to the following equations:

$$\text{Day: } T_s = b_0 + b_1 T_{11} + b_2 \Delta T_{11-12} T_s^0 + b_3 \Delta T_{11-12} + b_4 \Delta T_{11-12} S_\theta, \quad (7)$$

A similar approach to optimization of the offset at T_s^0 was used by Hosoda et al. (2007) for SST retrieval from MODIS in the North West Pacific.

The nighttime NAVO equation takes the following form:

$$\text{Night: } T_s = a_0 + a_1 T_{11} + a_2 \Delta T_{3.7-12} T_s^0 + a_3 \Delta T_{3.7-12} + a_4 S_\theta. \quad (8)$$

2.7 NRL

McBride et al. [2013] of the Naval Research Laboratory (NRL) proposed stabilizing SST retrievals (especially at large VZAs) by explicitly including the first guess SST, T_s^0 , in the NLSST equation as a separate regressor. This led them to the following formulation of the daytime equation:

$$T_s = b_0 + b_1 T_{11} + b_2 \Delta T_{11-12} + b_3 \Delta T_{11-12} S_\theta + b_4 T_s^0. \quad (9)$$

2.8 SUMMARY OF SST ALGORITHMS

The daytime SST algorithms described in this section demonstrate two main trends in modifications of the NLSST approach: 1) representing regression coefficients as functions of some proxies of the atmospheric attenuation, including ΔT_{11-12} (Pathfinder, NASA-MODIS, and IDPS

algorithms), latitude and month (LATBAND) or VZA (OSI-SAF), and 2) different ways of accounting for the first guess SST T_s^0 . The ACSPO, Pathfinder, NASA-MODIS, and OSI-SAF daytime equations include the regressor ΔT_{11-12} ($T_s^0 - 273.15$). The IDPS algorithm uses the regressor $\Delta T_{11-12} T_s^0$. The NAVO algorithm includes the regressors $\Delta T_{11-12} T_s^0$ and ΔT_{11-12} , which is equivalent to adding an empirical offset to T_s^0 . In the NRL algorithm, T_s^0 is used as an additional regressor that is aimed at improving SST accuracy and precision by weighting the retrieved SST with a first guess in the solution

The nighttime regression SST algorithms also differ in the way that they use (or don't use) the band at 3.7 μm , which is more transparent than either split-window band, 11 or 12 μm . In the ACSPO equation (1) and the OSI-SAF equation (6), $T_{3.7}$ is included as a standalone regressor. On the other hand, the IDPS, LATBAND, and NAVO equations all use the $T_{3.7}$ only within the BT difference, $T_{3.7} - T_{12}$, whereas the nighttime Pathfinder equation does not use the $T_{3.7}$ at all, in an attempt to produce a more consistent product across day and night.

Note that the objective of this study was to compare and explore the SST equations used in different algorithms, by testing them under similar conditions, rather than to reproduce all specific details of the authors' implementations of the algorithms. For instance, we do not consider the difference in the cloud masking algorithms. We do not explore here the effect of spatial smoothing ΔT_{11-12} , used in the OSI-SAF algorithm to reduce the noise in the retrieved SST [OSI-SAF Low Earth Orbiter SST Product User Manual, 2009]. Likewise, the NRL algorithm, which stabilizes NLSST estimates by using the first guess SST as a regressor, was only tested with daytime data for comparisons with other NLSST algorithms.

3 SST RETRIEVAL CHARACTERISTICS

Customarily, accuracy and precision of satellite SST, T_S , is characterized with bias, B , and standard deviation (SD, σ) of T_S with respect to in situ SST, T_S^i , averaged over a dataset of matchups (MDS) of observed BTs and T_S^i . It has been shown recently, however, that these statistics may not be fully representative of the quality of SST estimate because small B and σ can be generally achieved at the expense of suppressing natural SST variability, and, in particular, underestimation of its diurnal variability and spatial gradients [Merchant et al., 2009a; Petrenko et al., 2011]. To quantitatively characterize the capability of satellite SST to reproduce true SST variations, Merchant et al. [2009b] proposed an additional metric, the sensitivity μ of retrieved SST to true SST. The μ is estimated by differentiating the algorithm's equation by SST with derivatives of T_B being calculated using RTM. The closer μ is to 1, the more accurately variations in retrieved SST reproduce the true magnitudes of SST variations. The set of three retrieval characteristics, B , σ , and μ was used in this study to characterize the quality of local SST estimates.

However, assessment of the overall algorithm performance is complicated by the fact that B , σ and μ are sensitive to observational conditions, and therefore, show significant spatial and temporal variability. Even if an SST product meets the global requirements (specifications) posed by various applications (climate, fishery, etc.) on retrieval characteristics, these specifications are not necessarily met at every observed element of the ocean surface. Evaluation of overall algorithm performance should account for favorability of spatial and temporal distributions of B , σ , and μ rather than global or regional averages of those metrics. Here, we introduce a new measure of the algorithm's performance, the Quality Retrieval Domain (QRD), which is defined as a part of the full

geographical SST domain in which predefined specifications on B , σ , and μ are met. We will show that, given specifications for B , σ , and μ , the QRD significantly varies for different SST algorithms, which makes this parameter informative for an algorithm's ranking. On the other hand, the optimality of an SST algorithm depends on the adopted specifications. Therefore, it is important to determine the specifications so as to satisfy the majority of potential applications of the SST product. Considering that the global VIIRS SST product should be useful for both climate studies, which customarily use averaged SST over space and time [e.g., Merchant et al., 2008a], as well as other applications that require the sensor's native temporal and spatial resolution (e.g., fishery, military etc., [Donlon et al., 2007]), the approach to the selection of specifications on the retrieval characteristics was formulated as follows.

1. In order to more fully explore the information content of VIIRS observations, we consider a full swath of VIIRS observations, $|\theta| \leq 70^\circ$.
2. The global VIIRS SST product should meet predefined specifications over most of the ocean, which means that QRD must be large enough. Therefore, we are seeking a reasonable tradeoff between the specifications on retrieval characteristics and the QRD, rather than predefining conservative specifications in advance.
3. The natural spatial (750 m at nadir) and temporal resolution of VIIRS observations must be preserved in the global VIIRS SST product. Therefore, the retrieval characteristics are estimated for one day of VIIRS observations and mapped using averaging over $0.8^\circ \times 0.8^\circ$ latitude/longitude (lat/lon) cells. Note that at high latitudes mapping can involve averaging of several observations made at different VZAs from neighboring orbits. We expect that this averaging only minimally

effects local estimates of retrieval characteristics because, as will be shown in Section 5, angular dependencies of B , σ , and μ are relatively flat at lower atmospheric attenuations.

4 EVALUATION OF RETRIEVAL CHARACTERISTICS

The QRDs for all tested algorithms were estimated from one day of VIIRS observations processed with ACSPO. This required B , σ , and μ to be estimated at every observed element of the ocean surface. The pixel values of μ were calculated within ACSPO with CRTM. The pixel values of B and σ were produced from the MDS collected at STAR since April 2012. The MDS includes matchups of VIIRS BTs in bands M12 (3.7 μm), M15 (10.8 μm), and M16 (12 μm) with in situ SSTs obtained from the in situ Quality Monitor (*iQuam*; [Xu and Ignatov, 2013], available at www.star.nesdis.noaa.gov/sod/sst/iquam/). Only drifter's and tropical moored buoy's matchups were used. The time interval between *in situ* and satellite measurements was limited with 2hrs, and the distances between the buoy locations and the nearest clear-sky pixel were < 10 km. Satellite level 1b data were processed with the ACSPO, which allowed selecting clear-sky matchups with the ACSPO Clear-Sky Mask (ACSM) [Petrenko et al., 2010]. and to supply the matchups with VZAs, a priori SST T_s^0 , and total precipitable water vapor content in the atmosphere (TPW, W). ACSPO obtains T_s^0 and W from gridded DSST and National Center for Environmental Prediction (NCEP) Global Forecast System (GFS, available at www.nco.ncep.noaa.gov/pmb/products/gfs/) products, respectively. T_s^0 and W , interpolated from native grids to sensors' pixels, are reported in the output ACSPO L2 files and saved in the MDS.

The pixel values of B and σ were calculated for a single day of VIIRS observations as follows.

First, regression coefficients for all tested algorithms were derived from MDS acquired during a certain time period, and SSTs were estimated for all matchups within this MDS using the corresponding regression equations. After that, 2D look-up tables (LUT) were created, in which B and σ were represented as functions of VZA and TPW by averaging $T_S - T_S^i$ within 10° VZA \times 10 kg/m² TPW boxes. As an example, Fig. 1 shows the composite maps of TPW and VZA for daytime VIIRS observations on 24 August 2012. Finally, the pixel values of B and σ were derived by interpolation of LUT to pixel values of VZA and TPW. The LUTs of sensitivities, similar to LUTs of B and σ , were produced from pixel values of μ , calculated for the same day with the ACSPO using CRTM BT derivatives.

The pixel values of B , σ and μ were used to produce composite maps of QRD for all tested algorithms. Based on the maps of B , σ , and μ and predefined specifications on these characteristics, the QRD for every algorithm was determined as follows:

$$QRD = N_1 / N_2. \quad (10)$$

Here, N_1 is the number of $0.8^\circ \times 0.8^\circ$ lat/lon cells for which the mapped values of B , σ , and μ are all within the specifications, and N_2 is the total number of observed ocean cells.

In order to evaluate the stability of QRD estimates and overall ranking of the SST algorithms, the procedures described above were performed for two days of VIIRS observations, 24 August 2012 (Day 1) and 4 January 2014 (Day 2), using two MDS of matchups. The first MDS (MDS 1) included 64,653 daytime and 69,653 nighttime matchups collected from 15 April 2012 through 14 February 2013, whereas the second MDS (MDS 2) included 69,630 daytime matchups and 73,862

nighttime matchups, acquired from March 15 2013 through January 15 2014. Sections 5 and 6 contain a comparative analysis of retrieval metrics and QRDs produced with MDS 1 for Day 1. Other combinations of MDS and VIIRS observations (MDS 1 and Day2; MDS 2 and Day1; MDS 2 and Day 2) are used to verify the stability of QRD estimates and the algorithms' ranking resulted from this analysis.

5 ASSESSMENT OF DAYTIME SST ALGORITHMS

The matchups of VIIRS BTs and in situ SST acquired from 15 April 2012 through 14 February 2013 (MDS 1) were used to calculate regression coefficients and LUTs of B and σ for all tested algorithms.

Table 2 shows average biases and SDs of $T_S - T_S^i$ for daytime algorithms arranged in the order of increasing SDs. The SD for NRL SST is much smaller than for other algorithms. This is the result of using T_S^0 as a regressor in equation (9). Recall that T_S^0 is obtained by blending satellite retrievals with in situ data, and therefore may fit T_S^i more closely than satellite retrievals alone [e.g., O'Carroll et al., 2008; Xu and Ignatov, 2010]. As a result, the NRL SST best coincides with in situ SST, but this is achieved at the expense of least sensitivity to true SST, as shown later in this section. Out of all other algorithms, the lowest SD is produced by the OSI-SAF followed by the LATBAND and Pathfinder. The NAVO algorithm, whose equation (7) includes an adjustable offset at T_S^0 , slightly outperforms ACSPO which exploits the standard NLSST equation (2) with first guess SST in Celsius. The largest SD is delivered by the IDPS algorithm whose equation is similar to equations (3, a-e), but uses T_S^0 in kelvin rather than in Celsius.

Fig. 2 shows LUT biases as functions of VZA at six values of TPW for daytime algorithms. For the OSI-SAF, the bias never exceeds 0.1 K and is remarkably more uniform than for all other algorithms. The only exception is the NRL algorithm, which also produces relatively flat biases. This is because the NRL SST is largely dominated by the first guess SST, which does not depend upon VZA, whereas satellite SST may vary with VZA to a degree, depending upon the retrieval algorithm. For other algorithms, the biases are more variable with the shapes of angular dependencies being different for different TPWs. When interpreting Fig.2 quantitatively, one should bear in mind that the typical uncertainty of each point is $\sim 0.02\text{K}$ at a 95% statistical significance level, according to the Student's T-test.

Fig. 3 shows LUT SDs as functions of VZA at six TPW values. The effect of the first guess SST flattens out the dependencies of SD for the NRL SST. For other algorithms, the shapes of the curves are similar. Typically, SD increases with TPW and VZA, especially at $|\theta| > 40^\circ$ and at large TPWs. Consistent with Table 2, the smallest SDs are produced by the OSI-SAF algorithm, and the largest SDs correspond to the IDPS algorithm. As for biases in Fig. 2, the variations in SDs observed in Fig.3 are systematically and statistically significantly larger than their corresponding uncertainties (according to the F-test, $\sim 0.03\text{K}$ at a 95% statistical significance).

Fig. 4 plots sensitivities of retrieved SST to true SST as functions of VZA binned by TPW. For the same VZAs and TPWs, the values of μ can significantly differ for different algorithms. For example, the values of μ for the LATBAND at large TPWs are smaller than for all other algorithms, except NRL. Generally, μ decreases with VZA and TPW. However, for $\text{TPW} < 10\text{--}30 \text{ kg/m}^2$, μ may increase slightly towards larger VZAs, depending on the algorithm. This increase is especially

noticeable for the IDPS algorithm at $TPW < 20 \text{ kg/m}^2$, where μ exceeds 1.1 for $|\theta| > 60^\circ$. Fig. 4 also shows that the sensitivity of NRL SST to true SST does not exceed 0.4 (the remaining ~0.6 is sensitivity to the first guess SST). This means that the NRL algorithm reproduces no more than 40% of true magnitudes of SST variations in time (due to e.g. diurnal cycle) or space (e.g., thermal fronts and other SST contrasts on the surface).

Comparison of Figs. 3 and 4 suggests that, generally, sensitivity decreases with the atmospheric absorption, whereas the SD increases. However, the relationships between retrieval characteristics are not identical for different algorithms. Fig. 5 shows dependencies of average B , σ , and μ on TPW measured along slant atmospheric path (STPW):

$$STPW = W \times \sec\theta. \quad (10)$$

Fig. 5a shows that, consistent with Fig. 2, the OSI-SAF SST bias is least variable with STPW. Unlike the biases of all other algorithms (except NRL), the OSI-SAF SST bias remains stable even at $STPW > 100 \text{ kg/m}^2$. The SDs for all algorithms increase with STPW (Fig. 5b), whereas the sensitivities always decrease (Fig. 5c). The smallest SD is for the NRL algorithm, but it is accompanied by an unacceptable low sensitivity to true SST. For all other algorithms, the OSI-SAF SDs tend to fall at the lowest envelope, with the IDPS SDs bracketing the family from above. At the same time, the sensitivity of OSI-SAF SST at moderate atmospheric conditions ($STPW < 60 \text{ kg/m}^2$) is higher than for ACSPO, Pathfinder, NAVO, or LATBAND. Under more stringent atmospheric conditions ($STPW > 60 \text{ kg/m}^2$), the sensitivity of the OSI-SAF SST is lower than ACSPO, NAVO, and Pathfinder, but SD also remains the lowest. Overall, in addition to the most uniform bias, the OSI-SAF algorithm is deemed to provide the best tradeoff between SD and sensitivity to true SST.

It is instructive to compare the sensitivities of the LATBAND, Pathfinder and ACSPO algorithms, using the same equation (2). The sensitivity of LATBAND in Fig. 5c is lower than for Pathfinder and ACSPO. This is a consequence of subsetting matchups for separate calculation of the LATBAND coefficients for different latitudinal bands and months. Variations in true SST within each subset of matchups are much lower than within the whole MDS. This, in turn, causes underestimation of regression coefficients and reduces sensitivity of LATBAND SST to true SST variations. This effect was described by [Petrenko et al., 2011] with regard to development of the Incremental Regression algorithm.

Significant dependencies on atmospheric attenuation make the retrieval characteristics highly variable in space. Figs. 6-8 show the composite maps of B , σ , and μ for 24 August 2012 (note that the maps for NRL SST are not shown; due to its extremely low sensitivity to true SST, NRL SST was excluded from all further analyses in this paper). In Fig. 6, variability of B is smallest for the OSI-SAF, with $B \leq 0.1$ K. Fig. 7 shows composite maps of estimated SDs. Consistent with Figs. 1b and 3, retrievals with $TPW > \sim 45\text{-}50 \text{ kg/m}^2$ tend to have larger SDs, especially at the swath edges with larger VZAs. Fig. 8 shows composite maps of μ . Values of $\mu \sim 1$ are mainly observed at the high latitudes with low TPWs. Sensitivities for LATBAND are typically lower than for other algorithms for the same geographical regions. Especially low LATBAND sensitivities (0.4 to 0.6 across the swath) take place within the latitudinal band $0^\circ\text{-}20^\circ\text{N}$. For other algorithms, in the regions with $TPWs > 40\text{-}50 \text{ kg/m}^2$, μ decreases to 0.8-0.9 at the center of the swath, and further to 0.4-0.5 at swath edges.

The spatial distributions of B , σ , and μ shown in Figs. 6-8 allow determination of QRD for specified combinations of retrieval characteristics. As an example, Fig. 9 shows geographic distributions of quality SST retrievals from VIIRS observations, corresponding to the following specifications: $|B| < 0.1$ K; $\sigma < 0.4$ K; and $0.8 < \mu < 1.1$. The QRDs for all algorithms exclude regions with large TPW observed at large VZAs (cf. Fig. 1). All algorithms, except for OSI-SAF, often exclude the tropical regions (with large TPWs) even when observed at near-nadir VZAs due to higher variability of biases (cf. Fig. 2). The QRDs for ACSPO, LATBAND and NAVO algorithms additionally exclude some areas observed at smaller VZAs in the Southern Hemisphere. The QRD for IDPS excludes the areas with small TPWs and large VZAs where μ exceeds 1.1. Overall, under the same specifications, the QRDs for different SST algorithms are significantly different, thus confirming that it is an informative characteristic of the algorithm's performance.

Table 3 summarizes QRDs for six daytime algorithms, for two specifications on B , three specifications on σ , and three specifications on μ . The most significant factor affecting QRD is μ . With the most stringent specifications on μ ($0.9 < \mu < 1.1$), the greatest QRD is provided by the IDPS algorithm, except when $|B| < 0.2$ K and $\sigma < 0.4$ K, in which case NAVO covers a larger area. However, in this case, the maximum QRD does not exceed 65%. With less stringent specifications on μ , the optimal algorithm is mainly defined by the specifications on B and σ . If those are relaxed to $|B| < 0.2$ K and $\sigma < 0.5$ - 0.6 K, then the maximum QRD is provided by the NAVO algorithm. With more stringent specifications ($|B| < 0.1$ K or $|B| < 0.2$ K and $\sigma < 0.4$ K), the optimal SST algorithm is OSI-SAF.

The optimal daytime algorithm for VIIRS was selected under the following assumptions:

1. Quality SST retrievals algorithm should cover a significant fraction of the global ocean; we selected 80% as a reasonable lower limit for the QRD.
2. The higher limit for SST bias is selected as 0.1 K, consistent with typical requirements posed by climate applications [e.g., Merchant et al., 2008a].

Based on these assumptions and data of Table 3, we have selected the OSI-SAF algorithm given by equation (4) for VIIRS. If different yet realistic combinations of requirements are considered, other SST formulations may provide comparable, or even slightly superior, combination of sensitivity, accuracy and precision. However, in all cases, the OSI SAF equations appear to work reasonably well, for a wide variety of SST applications.

The above conclusion on the superiority of the daytime OSI-SAF algorithm was made based on QRD estimates produced from the MDS 1 and VIIRS observations for a single day 24 August 2012 (Day 1). In general, the estimates of QRD may vary for different MDS used for calculation of LUTs of B and σ as well as depending on variations in a geographical distribution of TPW for different days. To verify that the ranking of the algorithms is stable with respect the above factors, we have performed similar estimations of QRD using combinations of MDS 1 and MDS 2 with Day 1 and Day 2 of VIIRS observations. Recall that the MDS 2 includes matchups collected from 15 March 2013 through 15 January 2014 and the Day 2 of VIIRS observations is 4 January 2014. For four combinations of two MDS and two observation days, Fig. 10 demonstrates the dependencies of QRDs on the specification on μ with the fixed specifications on B and σ : $|B| < 0.1$ K and $\sigma < 0.4$ K. Although the values of QRD for the same specifications may vary for different MDS and dates of observations, the ranking of the algorithms remains mostly the same in all four cases. In particular,

the QRD for the OSI-SAF algorithm is always the greatest for the less stringent specs $\mu > 0.7$ and $\mu > 0.8$. For the most stringent spec, $\mu > 0.9$, the OSI-SAF QRD is somewhat less than the IDPS QRD for Day 1 but somewhat greater than the IDPS QRD for Day 2. The OSI-SAF algorithm appears to be the optimal choice in all considered cases.

6 ASSESSMENT OF NIGHTTIME SST ALGORITHMS

A procedure similar to the one described in the previous section was applied to the evaluation of nighttime algorithms. Omitting the intermediate steps for brevity, we present the main results of this analysis. Table 4 shows the overall statistics of $T_S - T_S^i$ averaged over the ten-month MDS1. The algorithms are arranged in the order of decreasing SD. The smallest SDs are delivered by the OSI-SAF algorithm (5), which explicitly introduces the dependencies of regression coefficients on VZA, and by the LATBAND, which stratifies the coefficients of equation (4) into latitudinal bands and months. The largest SD corresponds to the Pathfinder algorithm. Interestingly, Pathfinder nighttime SD (0.54 K) is higher than daytime SD (0.48 K, according to Table 2). This fact has the following explanation. The matchups for the MDS used for algorithm evaluation were selected with the ACSPO Clear-Sky Mask, which is largely based on the analysis of retrieved SST [Petrenko et al., 2010]. The nighttime ACSPO equation (1) exploits three bands at 3.7, 11, and 12 μm , and, therefore, is less sensitive to variations in TPW and vertical profiles of water vapor than the Pathfinder, which uses only two bands at 11 and 12 μm during both day and night. Consequently, the nighttime VIIRS MDS includes matchups, which would have been rejected during the daytime, when the ACSPO uses the NLSST algorithm. This causes the increase of SD for the nighttime Pathfinder algorithm (3, a-e). This also confirms a known fact that at night, three-band algorithms are more efficient than

split-window algorithms [e.g., *Brisson et al.*, 1998]. Another observation from Table 4 is that three-band algorithms that use $T_{3.7}$ as a standalone regressor (OSI -SAF, ACSPO) are more precise than the algorithms that use $T_{3.7}$ only in the BT difference, $\Delta T_{3.7-12}$ (NAVO, IDPS). The LATBAND algorithm, which uses the same equation (4) as NAVO and IDPS algorithms, improves SD by using separate sets of coefficients for different latitudinal bands. However, as shown in Table 5, the OSI-SAF and ACSPO algorithms still outperform LATBAND in terms of spatial variations in B and μ .

Table 5 shows the QRDs, estimated for nighttime algorithms under the same specifications on B , σ , and μ as were used in Table 3 for daytime algorithms. In all cases, the two nighttime algorithms with the largest QRD are OSI-SAF and ACSPO. While the ACSPO performs better or similarly to OSI-SAF under relaxed specification on bias, $|B| < 0.2$ K, the OSI -SAF outperforms ACSPO when the specification on bias is more stringent ($|B| < 0.1$ K). Based on the same requirements as formulated in Section 5 for daytime algorithms, we recommend the nighttime OSI-SAF algorithm for the use with VIIRS data.

Fig. 11 demonstrates the dependencies of the QRD for six nighttime algorithms on the μ specification for combinations of two MDS with two days of VIIRS observations, with the same specs on B and σ , $|B| < 0.1$ K and $\sigma < 0.4$ K. The dependencies appear to be similar in all cases. The OSI-SAF algorithm always provides the largest QRDs if the minimum μ value is 0.7 or 0.8, and if the spec is $\mu > 0.9$ than the QRDs for OSI-SAF and ACSPO are very close. It follows from Fig. 11 that the nighttime OSI-SAF algorithm remains the optimal choice in all considered cases.

VALIDATION OF SST ALGORITHMS WITH IDPS AND ACSPO PRODUCTS

In Sections 5 and 6, the performances of SST algorithms were evaluated using a single dataset of matchups, selected with the ACSPO Clear-Sky Mask. However, overall performance of an L2 SST product depends not only on the SST algorithm, but also on its cloud mask. The cloud mask algorithms are different in IDPS and ACSPO. In ACSPO, the ACSM performs downstream of the SST algorithm, thus allowing direct control of the quality of retrieved SST [Petrenko et al., 2010]. The IDPS SST uses the upstream VIIRS Cloud Mask (VCM) [Hutchinson et al., 2011], which is independent from the SST algorithm. To quantify the extent to which the IDPS and ACSPO SST products can be improved by changing the SST algorithm only, the daytime and nighttime OSI-SAF algorithms were implemented within both systems and tested with one day of VIIRS observations, 29 October 2013. Table 6 presents the global bias and SD of deviations of IDPS and ACSPO SSTs from DSST, averaged over “confidently clear pixels” identified by each system as well as the corresponding number of such pixels. Due to inaccuracy in the DSST analysis resulting from gap filling and smoothing, the SDs of VIIRS SST–DSST are always larger than the SDs of VIIRS SST – in situ SST (cf. Tables 2 and 4). However, the differences between the SDs for ACSPO and IDPS shown in Table 6 are indicative of the relative performance of the two products. While the IDPS SST SDs are significantly larger than ACSPO SDs, the IDPS system produces only 1 to 3 % more confidently clear pixels during day and about 3% less confidently clear pixels during night. This suggests that the VCM is significantly less efficient than the ACSM. Replacing the original algorithms with the OSI-SAF algorithms reduces the SDs for both IDPS and ACSPO. However, even with the same OSI-SAF algorithms, the IDPS SDs remain much larger than ACSPO SDs. This suggests that further improvement of the IDPS SST product requires adjustment of the VCM.

Fig. 12 maps the differences between SSTs retrieved with the original and OSI-SAF algorithms. For consistency, all maps were produced with the same ACSM. Replacement of the SST algorithms significantly changes daytime IDPS SST at swath edges in mid-latitudes, whereas in the tropics and in the high latitudes changes in IDPS SST are significant over the full swath. The daytime ACSPO SST changes in a full swath in the tropics, and at swath edges in mid and high latitudes. The nighttime IDPS SST also changes due to the algorithm replacement, but to a lesser extent than the daytime SST. The changes in the nighttime ACSPO SST are most noticeable in the tropics and at scan edges.

8 SUMMARY AND DISCUSSION

The existing operational and proposed regression SST algorithms have been evaluated to select the global SST algorithm for VIIRS. The quality of SST retrievals was characterized with three parameters: bias and SD of retrieved SST, and its sensitivity to true SST. These retrieval characteristics were shown to be non-uniform functions of observational conditions, in particular, VZA and TPW, which in turn leads to their significant spatial variations. This suggests that globally average values of B , σ , and μ cannot be fully representative of the algorithm's performance over vast geographic regions. Rather, their spatial distributions should be considered. We have defined a new metric of the algorithm performance, the Quality Retrieval Domain (QRD), as a percentage of the valid SST domain in which B , σ , and μ meet predefined specifications. We have shown that under the same specifications posed on B , σ , and μ , QRD differs significantly for different retrieval algorithms, which makes it an informative characteristic of the algorithm's performance.

511 Furthermore, the selection of the optimal algorithm in terms of QRD is sensitive to specifications
512 posed on retrieval characteristics.

513 Comparison of daytime SST algorithms shows that accounting for dependencies of regression
514 coefficients on some proxies of the atmospheric absorption (such as VZA, ΔT_{11-12} , latitude) improves
515 precision of the basic split-window NLSST equation (2). However, explicit accounting for
516 dependencies of regression coefficients on VZA turns out to be more efficient way to improve the
517 algorithm's performance. The NLSST performance also depends on the way the first guess SST, T_S^0 ,
518 is used in the regression equation. Using T_S^0 in kelvin rather than in degrees Celsius within the
519 regressor ΔT_{11-12} results in degradation of the algorithm's performance, whereas introducing a
520 variable offset of T_S^0 slightly improves the NLSST precision as compared to using T_S^0 in Celsius.
521 Introducing T_S^0 as a separate regressor in the NLSST equation significantly improves SST precision,
522 but dramatically reduces its sensitivity to true SST. To that end, the recent trend in the SST
523 community towards increased use of first guess (downstream L4) SST in the upstream L2 production
524 should be accompanied with control of sensitivity of an SST algorithm to true SST to prevent the
525 reduction in sensitivity of L2 product to true SST and the increase of sensitivity to the very same L4
526 product, which relies on L2 as input, thus possibly leading to a detrimental feedback. Based on QRD
527 estimates for daytime algorithms presented in Table 3, we recommend the OSI-SAF algorithm for
528 global processing of daytime VIIRS observations.

529 Out of all tested nighttime algorithms, the two algorithms showing comparable performance
530 under all considered specifications are ACSPO and OSI-SAF. Both are MCSST type and use $T_{B3.7}$
531 μm band as a separate predictor as opposed to LATBAND, NAVO and IDPS, which use $T_{B3.7}$ as a

part of the differential regressor $\Delta T_{3.7-12} T_s^0$, and to the Pathfinder algorithm which does not use $T_{B3.7}$ at all. At the same time, the OSI-SAF algorithm provides the maximum QRD (90%-100%) under the strictest specifications posed on the SST bias. Therefore, we recommend the OSI-SAF algorithm for nighttime VIIRS SST retrievals.

The replacement of the original algorithms with the OSI-SAF algorithms within the IDPS system has improved the consistency between VIIRS SST and DSST. However, even with the more efficient SST algorithm, the IDPS SST product remains suboptimal due to excessively liberal VCM. Further improvement of the IDPS SST product requires adjustment of the VCM, or implementation of additional tests similar to those employed in the ACSM downstream of SST algorithm.

Using the QRD metric allows a more generalized specification of the algorithm's performance compared to those processing systems in which quality SST retrievals are only deemed possible within a limited range of VZA. For instance, in the NESDIS Main Unit Task system [Ignatov et al., 2004], which was the predecessor of ACSPO, SST from AVHRR was retrieved at $|\theta| < 53^\circ$, and all data with VZAs $53^\circ < |\theta| < 67^\circ$ were discarded. In the OSI-SAF MetOp-A AVHRR SST product, the range of high quality SST is limited to VZAs $|\theta| < 55^\circ$ [OSI-SAF Low Earth Orbiter SST Product User Manual, 2009]. In MYD28 and MOD28 SST products, derived from Aqua and Terra MODIS, respectively, SST retrievals at $|\theta| > 55^\circ$ are flagged as degraded quality [Franz, 2009]. In the IDPS VIIRS SST algorithm, the range of "High Quality" SSTs is even more restrictive, $|\theta| \leq 40^\circ$ [Jackson and Siebels, 2011]. In general, these limitations are consistent with rapid degradation of all retrieval characteristics at $|\theta| > 40^\circ$, as is clearly seen in Figs. 2-4. However, these figures also show that the rate of degradation strongly depends on the atmospheric attenuation along the vertical path.

At low atmospheric attenuations and large VZAs, the retrieval characteristics can be even better than at high atmospheric attenuations and near-nadir VZAs. This fact is illustrated in Fig. 9 which shows complicated forms of QRDs for daytime algorithms. For the OSI-SAF algorithm, for example, the QRD excludes observations at large VZA only in regions with relatively high TPW (cf. Fig.1). This suggests that using the same VZA cut-off at all atmospheric attenuations may result in a loss of quality SST retrievals in regions with lower atmospheric attenuation. A more adequate approach to restricting quality SST retrievals would be representing them as functions of the atmospheric attenuation along the slant line of sight rather than the VZA or TPW alone.

Overall, inefficient handling of the fundamental degradations of precision and sensitivity of retrieved SST to true SST with atmospheric attenuation appears to be the main limitation of the conventional regression approach. Further improvements in the performance of the regression SST from VIIRS will be explored before the J1 launch in 2017, including using new forms of SST equations (e.g., allowing regression coefficients to freely vary with the VZA, rather than forcing some of them to vary linearly with $\sec\theta$, and tabulating corresponding dependencies in LUTs, as in e.g. [Llewellyn-Jones et al, 1984] and exploring new VIIRS bands M13 and M14 centered at 4.05 μm and 8.55 μm , respectively. Also, further developments of RTM-based SST algorithms can provide more capabilities to control variations of retrieval characteristics across the retrieval domain in the interest of various SST applications, provided the remaining issues are addressed. The major challenge for operational application of RTM-based SST algorithms remains the correction of highly variable in space and in time model minus observation biases, which is a prerequisite for physical retrievals [e.g., *Merchant et al*, 2008b; *Merchant et al*, 2009a; *Le Borgne et al.*, 2011; *Petrenko et al.*, 2011].

575 **Acknowledgments**

576 This work was conducted under the JPSS Data Products and Algorithms Team (DPA) and
577 Geostationary Operational Environmental Satellite-R Series (GOES-R) Algorithm Working Group
578 (AWG) funded by the JPSS and GOES-R Program Offices, respectively. We thank JPSS Program
579 Scientist Mitch Goldberg and AWG Manager Jaime Daniels. Thanks also go to our NOAA
580 colleagues John Sapper, XingMing Liang, Feng Xu, and Denise Frey for assistance, discussions, and
581 feedback at its different stages. We also thank our JPSS SST colleagues, Peter Minnett, Bob Evans,
582 and Kay Kilpatrick (University of Miami), Doug May and Jean-Francois Cayula (NAVO), Bob
583 Arnone and Walton McBride (Navy Research Laboratory and University of Southern Mississippi),
584 and Pierre LeBorgne and Herve Roquet (EUMETSAT OSI-SAF) for providing their algorithms and
585 helpful discussions. Constructive comments by three anonymous reviewers have been instrumental
586 for the authors to rethink and rewrite this manuscript. We particularly thank one reviewer, who not
587 only suggested improvements to our analyses, but also provided specific examples and
588 demonstrations of how some of them may be implemented. The views, opinions, and findings
589 contained in this paper are those of the authors and should not be construed as an official NOAA or
590 US Government position, policy, or decision.

591

592

593

594 REFERENCES

- 595 Brisson, A., P. Le Borgne, and A. Marsuin (1998), Development of algorithms for SST
596 retrieval at O&SI SAF low and mid latitudes, CMS Rep. to EUMETSAT, 38 p.
597 <http://www.eumetsat.int/groups/pps/documents/document/002170.pdf>
- 598 Brisson, A., P. Le Borgne, and A. Marsouin (2002), Result of one year of preoperational
599 production of Sea Surface Temperatures from GOES-8, *J. Atmos. Oceanic Technol.*, **19** (10), 1638–
600 1652.
- 601 Brown, O. B., and P. J. Minnett, 1999: MODIS infrared sea surface temperature algorithm -
602 Algorithm Theoretical Basis Document (Version 2), 98pp. (available at
603 http://oceancolor.gsfc.nasa.gov/DOCS/atbd_mod25.pdf).
- 604 Cao, C., J. Xiong, S. Blonski, Q. Liu, S. Uprety, X. Shao, Y. Bai, and F. Weng (2013), Suomi
605 NPP VIIRS sensor data record verification, validation, and long-term performance monitoring, *J.*
606 *Geophys. Res.*, **118**, 1-15, doi:10.1002/2013JD020418.
- 607 Casey, K.S., T.B. Brandon, P. Cornillon, and R. Evans, (2010), The past, present and future of
608 the AVHRR Pathfinder program. *Oceanography from space*, Springer, DOI:10.1007/978-90-481-
609 5_16. http://www.nodc.noaa.gov/SatelliteData/pathfinder4km/OFS_21_Cas_09Dec2009.pdf
- 610 Cayula, J.-F., D. May, B. McKenzie, and K. Willis (2013). VIIRS derived SST at the Naval
611 Oceanographic Office: From evaluation to operations. SPIE Conf. on Defense and Security,
612 Baltimore, 26 Apr–1 May 2013, paper 8724-35.

- 613 Dash, P., Ignatov, A., Kihai, Y., Sapper, J. (2010), The SST Quality Monitor (SQUAM), *JTech*,
614 **27**, 1899–1917. doi: 10.1175/2010JTECHO756.1.
- 615 Donlon, C., N. Rayner, I. Robinson, et al. (2007), The Global Ocean Data Assimilation
616 Experiment High-resolution Sea Surface Temperature Pilot Project, *Bull. Am. Meteorol. Soc.*, **88**,
617 1197–1213.
- 618 Donlon, C., M. Martin, J. Stark, J. Roberts-Jones, E. Fiedler, and W. Wimmer, (2012), The
619 operational sea surface temperature and Sea Ice Analysis (OSTIA) system. *Remote Sens. Environ.*,
620 **116**, 140–158
- 621 Evans, R., and G. Podesta, (1998), Pathfinder sea surface temperature algorithm. U. of Miami,
622 Rosentiel School of Marine and Atmospheric Science,
623 http://yyy.rsmas.miami.edu/groups/rrsl/pathfinder/Algorithm/algo_index.html.
- 624 Franz, B. (2006), Implementation of SST Processing within the OBPG.
625 http://oceancolor.gsfc.nasa.gov/DOCS/modis_sst/
- 626 Hosoda, K., H. Murakami, F. Sakaida and H. Kawamura (2007), Algorithm and validation of
627 sea surface temperature observation using MODIS sensors aboard Terra and Aqua in the Western
628 North Pacific. *Journal of Oceanography*, **53**(2), 267-280, doi:10.1007/s10872-007-0027-4.
- 629 Hutchinson, K.D., J. Roskovensky, J. Jackson et al. (2011). VIIRS Cloud Mask (VCM)
630 algorithm theoretical basis document ATBD (ref Y2412),
631 [http://www.star.nesdis.noaa.gov/jpss/documents/ATBD/GSFC_474-](http://www.star.nesdis.noaa.gov/jpss/documents/ATBD/GSFC_474-00033_JPSS_VIIRS_Cloud_Mask_ATBD_Alt_doc_no_D43766_Y2412_.pdf)
632 [00033_JPSS_VIIRS_Cloud_Mask_ATBD_Alt_doc_no_D43766_Y2412_.pdf](http://www.star.nesdis.noaa.gov/jpss/documents/ATBD/GSFC_474-00033_JPSS_VIIRS_Cloud_Mask_ATBD_Alt_doc_no_D43766_Y2412_.pdf)

633 Ignatov, A., J. Sapper, I. Laszlo et al., (2004), Global operational SST and aerosol products
634 from AVHRR: current status, diagnostics, and potential enhancements. 13th Conf. Satellite
635 Meteorology and Oceanography, Norfolk, VA, 20-23 September 2004.
636 [http://www.star.nesdis.noaa.gov/smcd/emb/aerosol/ignatov/conf/2004-AMS-13ConfSatMetOcean-](http://www.star.nesdis.noaa.gov/smcd/emb/aerosol/ignatov/conf/2004-AMS-13ConfSatMetOcean-IgnatovEtAl-AVHRRSSTAerosol-Poster.pdf)
637 [IgnatovEtAl-AVHRRSSTAerosol-Poster.pdf](http://www.star.nesdis.noaa.gov/smcd/emb/aerosol/ignatov/conf/2004-AMS-13ConfSatMetOcean-IgnatovEtAl-AVHRRSSTAerosol-Poster.pdf)

638 Ignatov A., X. Liang, P. Dash, et al., (2011), Joint Polar Satellite System (JPSS) SST Algorithm
639 and Cal/Val Activities at NESDIS/STAR. 2nd NASA SST Science Team Meeting, 2-4 November,
640 Miami Beach, FL.
641 http://sstscienceteam.org/Ignatov%202011_11_02_16_30_JPSS_SST_Ignatov.pdf

642 Ignatov A., J. Sapper, Y. Kihai, et al., (2012), Polar SST Products and Monitoring at NESDIS.
643 13th GHRSSST meeting, 4-8 June 2012, Tokyo, Japan.
644 [https://www.ghrsst.org/files/download.php?m=documents&f=120611145909-](https://www.ghrsst.org/files/download.php?m=documents&f=120611145909-1120120604ACSPOMonitoringIgnatovv04.pdf)
645 [1120120604ACSPOMonitoringIgnatovv04.pdf](https://www.ghrsst.org/files/download.php?m=documents&f=120611145909-1120120604ACSPOMonitoringIgnatovv04.pdf)

646 Jackson, S., and P.D. Siebels (2011), Operational Algorithm Description Document for VIIRS
647 Sea Surface Temperature (SST) EDR,
648 [http://npp.gsfc.nasa.gov/science/sciencedocuments/022012/474-00061_OAD-VIIRS-SST-EDR-](http://npp.gsfc.nasa.gov/science/sciencedocuments/022012/474-00061_OAD-VIIRS-SST-EDR-SW_RevA_20120127.pdf)
649 [SW_RevA_20120127.pdf](http://npp.gsfc.nasa.gov/science/sciencedocuments/022012/474-00061_OAD-VIIRS-SST-EDR-SW_RevA_20120127.pdf).

650 Kilpatrick, K.A., G.P. Podesta, and R. Evans (2001), Overview of the NOAA/NASA advanced
651 very high resolution radiometer Pathfinder algorithm for sea surface temperature and associated
652 matchup database, *J. Geophys. Res.*, **106**, C5, 9179-9297.

- 653 Lavanant, L., P. Le Borgne, G. Legendre, A. Marsouin, S. Pere, and H. Roquet (2012), VIIRS
654 SST at OSI-SAF. GHRSSST XIII Science Team Meeting, Tokyo, Japan
655 <https://www.ghrsst.org/files/download.php?m=documents&f=120618134746->
656 [GHRSSSTXIIIviirsosisaf3.pdf](https://www.ghrsst.org/files/download.php?m=documents&f=120618134746-GHRSSSTXIIIviirsosisaf3.pdf)
- 657 Le Borgne, P., H. Roquet, and C.J. Merchant (2011), Estimation of sea surface temperature
658 from the Spinning Enhanced Visible and Infrared Imager, improved using numerical weather
659 prediction, *Remote Sens. Environ.*, **115**, 55–65.
- 660 Liang, X., A. Ignatov, and Y. Kihai (2009), Implementation of the Community Radiative
661 Transfer Model (CRTM) in Advanced Clear-Sky Processor for Oceans (ACSPO) and validation
662 against nighttime radiances. *J. Geophys. Res.*, **114**, D06112, doi: 10.1029/2008JD010960.
- 663 Liang, X., and A. Ignatov (2011), Monitoring of IR Clear-sky Radiances over Oceans for SST
664 (MICROS). *J. Atmos. Ocean. Technol.*, **28**, doi:10.1175/JTECH-D-10-05023.1.
- 665 Liang, X. and A. Ignatov (2013), AVHRR, MODIS and VIIRS radiometric stability and
666 consistency in SST bands, *J. Geophys. Res.*, **118**, 6, 3161-3171, DOI: 10.1002/jgrc.20205.
- 667 Llewellyn-Jones, D.T., P.J. Minnett, R.W. Saunders, and A.M. Zavody (1984), Satellite multi-
668 channel infrared measurements of sea surface temperature of the N.E. Atlantic Ocean using
669 AVHRR/2, *Quart. J. R. Met. Soc.*, **110**, 613-631.
- 670 McBride, W., B.A. Arnone, and J.-F. Cayula (2013), Improvements of satellite SST retrievals at
671 full swath, SPIE Conf. on Defense and Security, Baltimore, 26 April–1 May 2013, paper 8724-36.

- 672 McClain, E.P., W.G. Pichel, and C.C. Walton (1985), Comparative performance of AVHRR-
673 based multichannel sea surface temperature, *J. Geophys. Res.*, **90**, C6, 11,587-11,601.
674 doi:10.1029/JC090iC06p11587.
- 675 Merchant, C. J., D. Llewellyn-Jones, R.W. Saunders, N.A. Rayner, E.C. Kent, C.P. Old, D.
676 Berry, A.R. Birks, T. Blackmore, G.K. Corlett, O. Embury, V.L. Jay, J. Kennedy, C.T. Mutlow, T.J.
677 Nightingale, A.G. O'Carroll, M.J. Pritchard, J.J. Remedios, and S. Tett (2008a), Deriving a sea
678 surface temperature record suitable for climate change research from the along-track scanning
679 radiometers, *Advances in Space Research*, **41**, 1, 1-11.
- 680 Merchant C J, P Le Borgne, A Marsouin and H Roquet (2008b), Optimal estimation of
681 sea surface temperature from split-window observations, *Remote. Sens. Environ.*, 112 (5),
682 2469-2484. doi:10.1016/j.rse.2007.11.011
- 683 Merchant, C. J., P. Le Borgne, P., H. Roquet, and A. Marsouin (2009a), Sea surface temperature
684 from a geostationary satellite by optimal estimation, *Remote Sens. Environ.*, **113**, 445–457.
- 685 Merchant, C.J., A.R. Harris, H. Roquet, and P. Le Borgne (2009b), Retrieval characteristics of
686 non-linear sea surface temperature from the Advanced Very High Resolution Radiometer, *Geophys.*
687 *Res. Lett.*, **36**, L17604, doi: 10.1029/2009GL039843.
- 688 Minnett, P.J., O.B. Brown, R.H. Evans, E.L. Key, E.J. Kearns, K. Kilpatrick, A. Kumar, K.A.
689 Maillet, and G. Szczodrak (2004), Sea-surface temperature measurements from the Moderate-
690 Resolution Imaging Spectroradiometer (MODIS) on Aqua and Terra, Geoscience and Remote
691 Sensing Symposium, Proc. IGARSS '04, 7, 4576–4579.

- 692 Minnett, P.J., and R.H. Evans (2009), MODIS sea-surface temperatures. GHRSSST User
693 Symposium, Santa Rosa, CA, USA, 28-29 May 2009,
694 https://www.ghrsst.org/files/download.php?m=documents&f=Session2_Minnett.ppt
- 695 O'Carroll, A.G., J.R. Eyre and R.W. Saunders (2008), Three-way error analysis between AATSR,
696 AMSR-E and in situ sea surface temperature observations, *JTech*, **25**, 1197–1207.
- 697 OSI-SAF Low Earth Orbiter Sea Surface Temperature Product User Manual, Version 2.1. The
698 EUMETSAT Network of Satellite Application Facilities, OSI-SAF (2009),
699 http://www.osi-saf.org/biblio/docs/ss1_pum_leo_sst_2_1.pdf
- 700 Petrenko, B., A. Ignatov, Y. Kihai, and A. Heidinger (2010), Clear-sky mask for the Advanced
701 Clear-Sky Processor for Oceans, *JTech*, **27**, 1609–1623.
- 702 Petrenko, B., A. Ignatov, N. Shabanov, and Y. Kihai (2011), Development and evaluation of
703 SST algorithms for GOES-R ABI using MSG SEVIRI as a proxy, *Remote Sens. Environ.*, **115**,
704 3647–3658.
- 705 Reynolds, R.W., T.M. Smith, C. Liu, C., D.B. Chelton, K.S. Casey, and M.G. Schlax (2007),
706 Daily high-resolution-blended analyses for sea surface temperature, *J. Clim.*, **20**, 5473–5496.
- 707 Walton, C.C., W.G. Pichel, J.F. Sapper, and D.A. May (1998), The development and
708 operational application of nonlinear algorithms for the sea surface temperatures with the NOAA
709 polar-orbiting environmental satellites, *J. Geophys. Res.*, **103**, 27999–28012.
- 710 Xu, F., and A. Ignatov (2010), Evaluation of in situ SSTs for use in the calibration and
711 validation of satellite retrievals, *J. Geoph. Res.*, **115**, C09022, doi:10.1029/2010JC006129.

712 Xu, F., and A. Ignatov (2013), In situ SST Quality Monitor (*iQuam*), *JTech*,
713 doi:10.1175/JTECH-D-13-00121.1, in press.

714

715

716

717

718

719

720

721

FIGURES

722

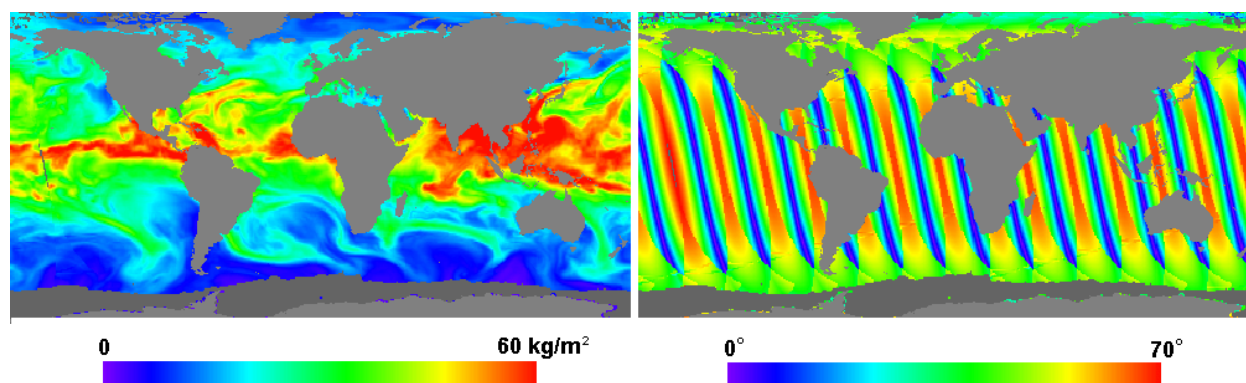


Fig. 1. Composite maps of (left) TPW and (right) absolute value of VZA for daytime VIIRS observations on 24 August 2012.

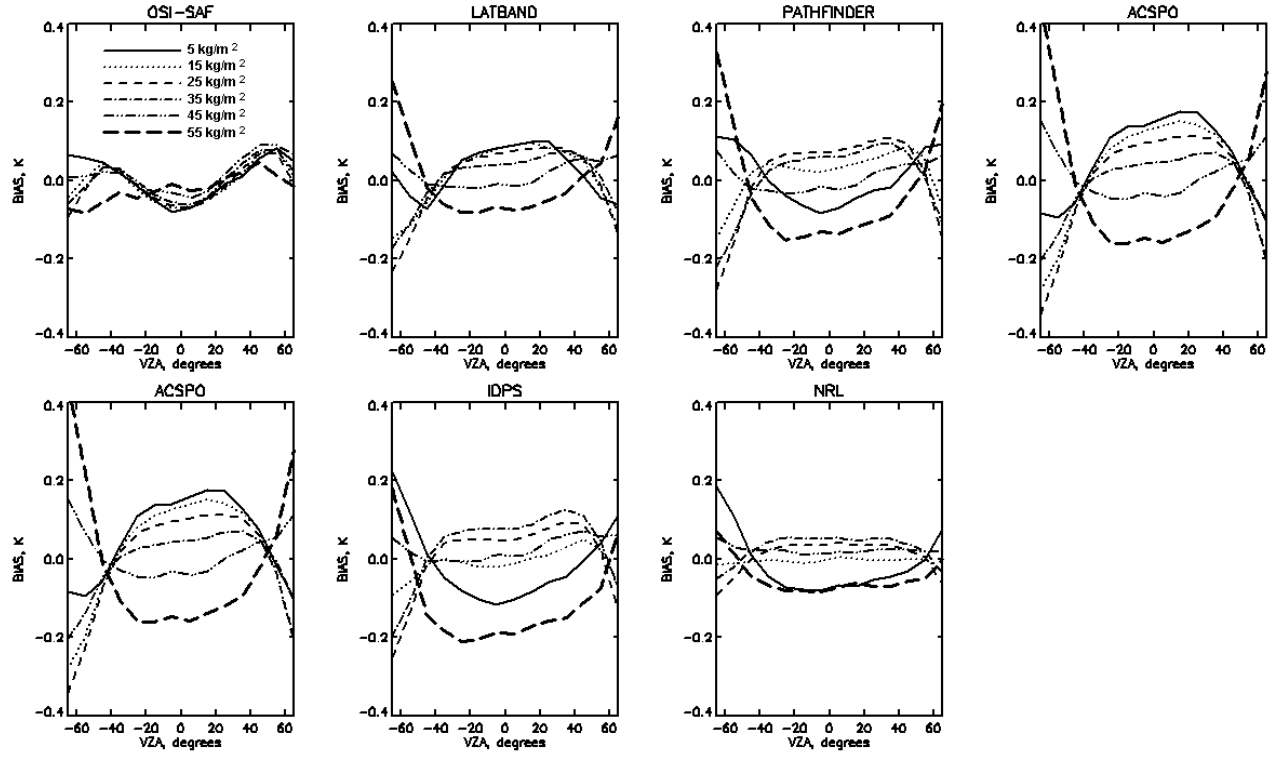


Fig. 2. Biases of $T_S - T_S^i$ as functions of VZA at six values of TPW, averaged from 10 months of VIIRS MDS for daytime SST algorithms.

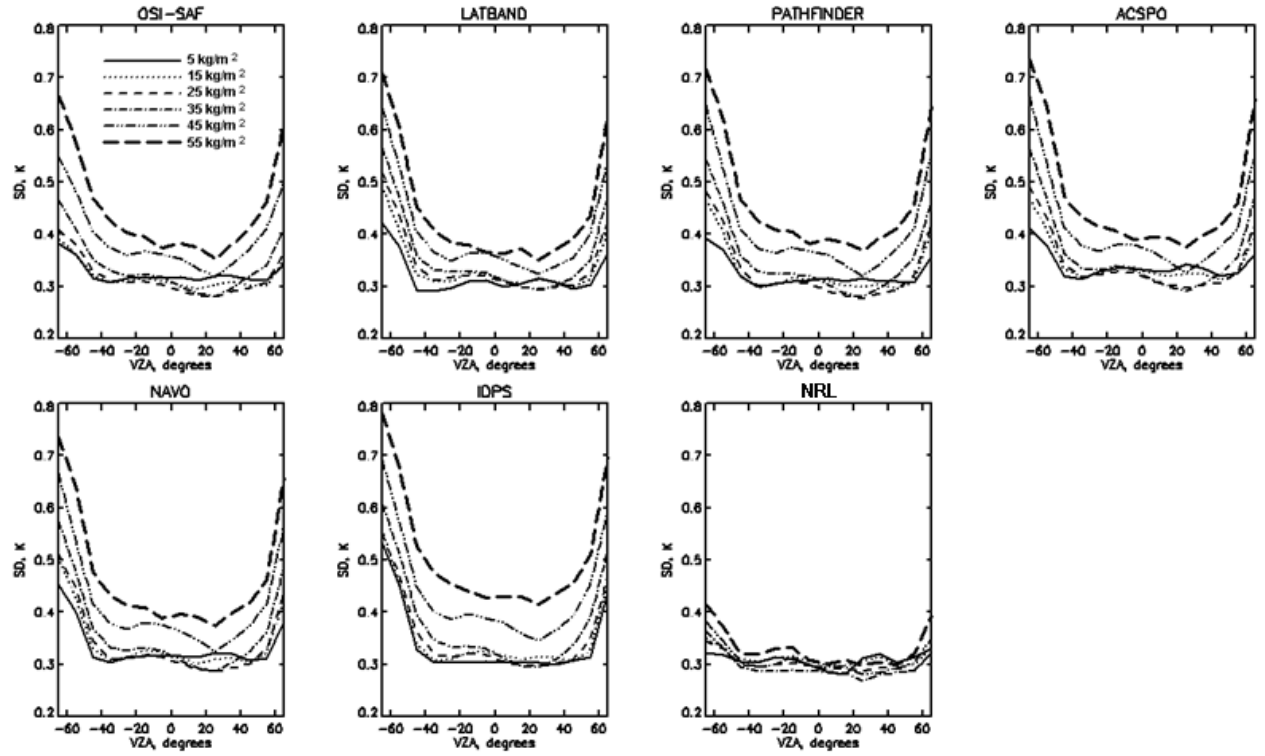


Fig. 3. SD of $T_S - T_S^i$ as functions of VZA at six values of TPW, averaged from 10 months of VIIRS MDS for daytime SST algorithms.

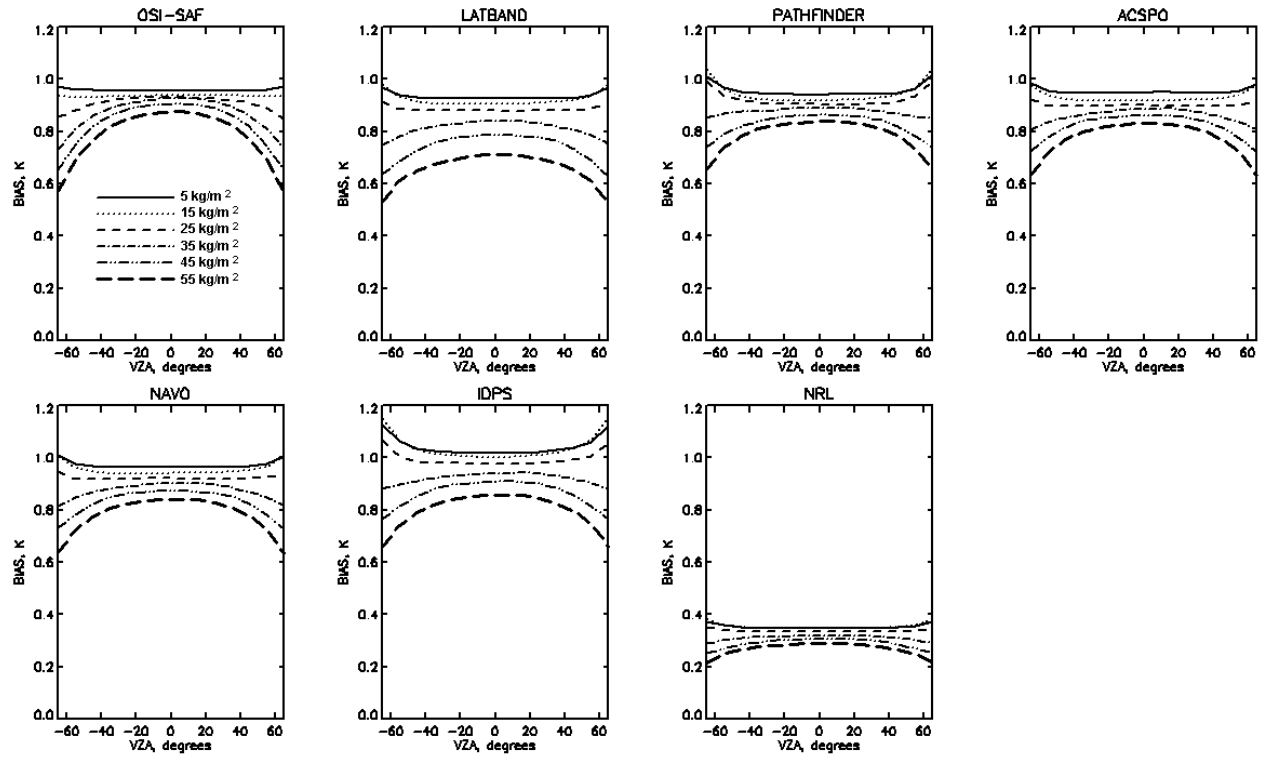


Fig. 4. Sensitivities of retrieved SST to true SST as functions of VZA at six values of TPW, for daytime SST algorithms.

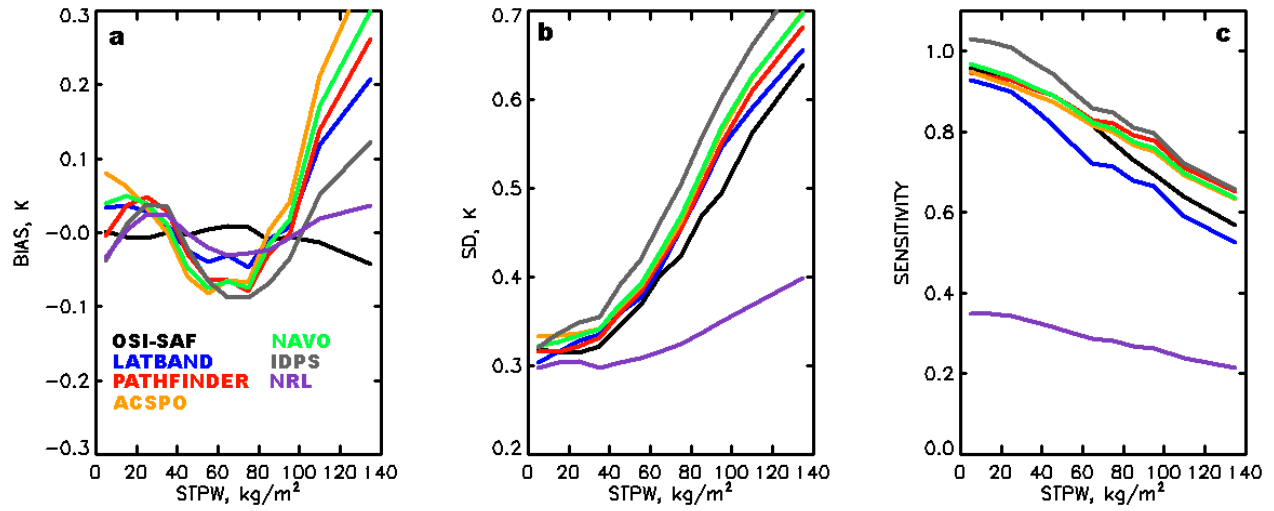


Fig. 5. (a) Bias and (b) SD of $T_S - T_S^i$ and (c) sensitivity of T_S to true SST as functions of TPW along the slant path for daytime SST algorithms.

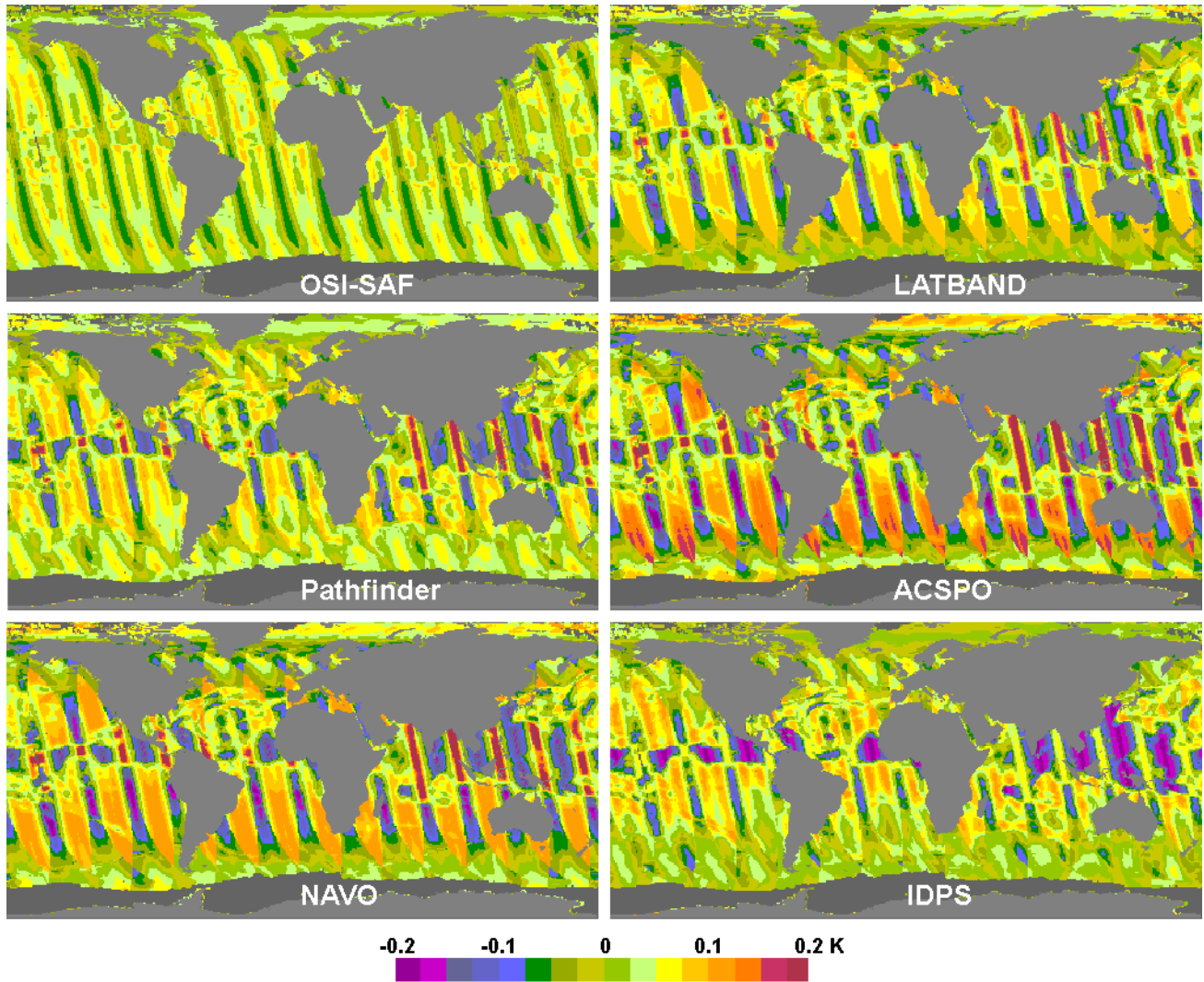


Fig. 6. Composite maps of estimated bias in retrieved SST for six daytime SST algorithms for 24 August 2012.

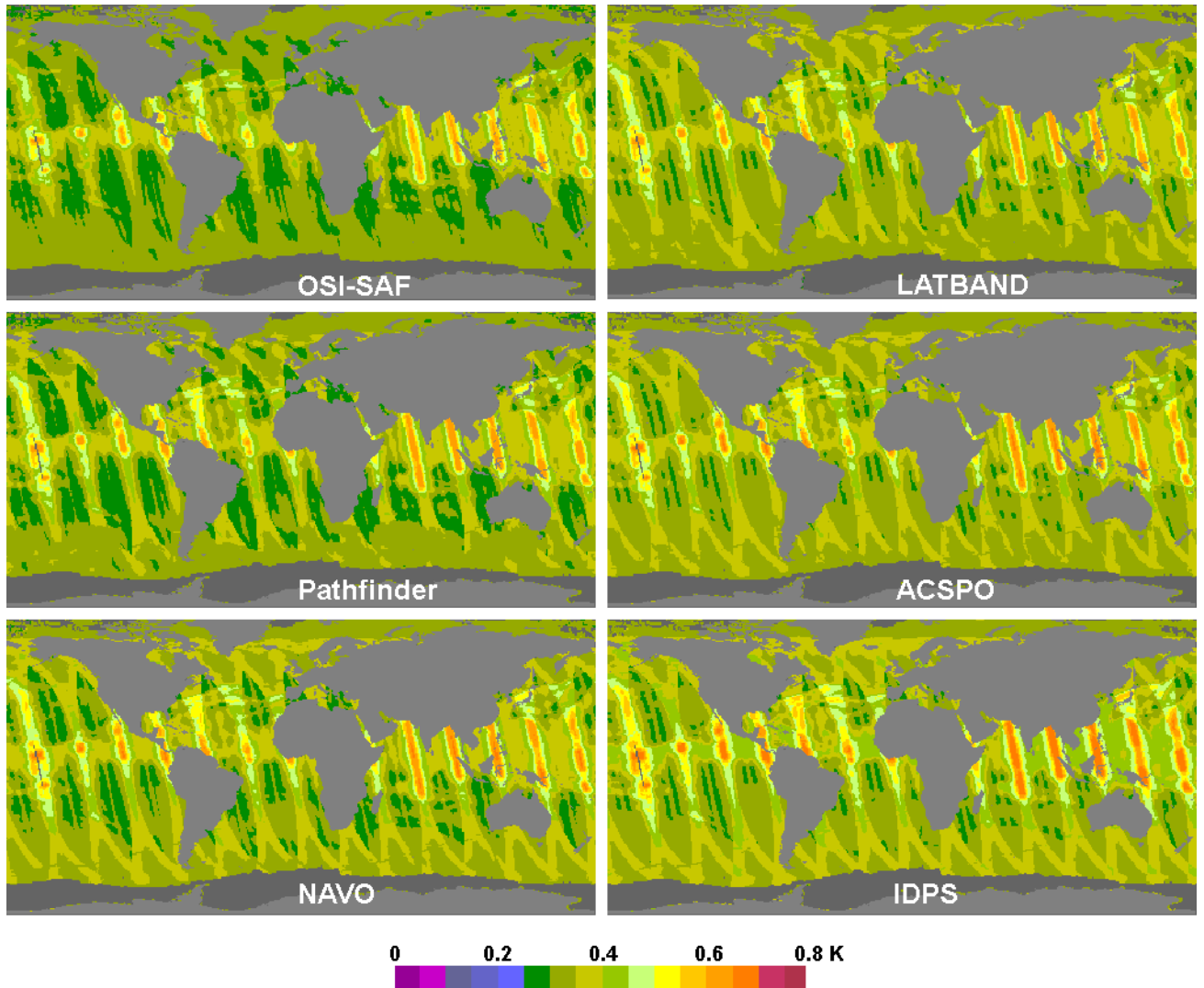


Fig. 7. Composite maps of estimated SD in retrieved SST for six daytime SST algorithms for 24 August 2012.

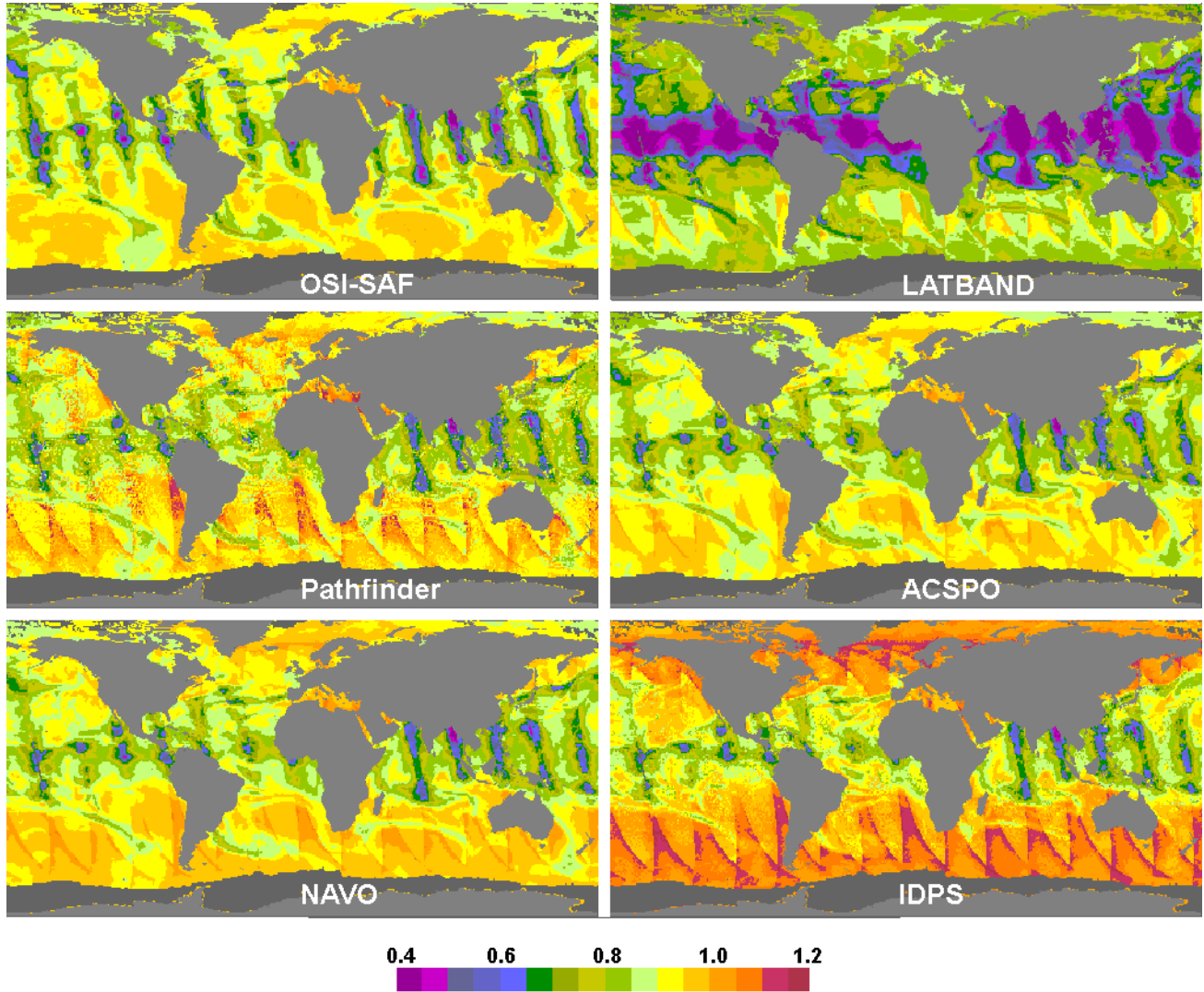


Fig. 8. Composite maps of sensitivities of retrieved SST to true SST produced from pixel sensitivity values for 24 August 2012 for six daytime algorithms.

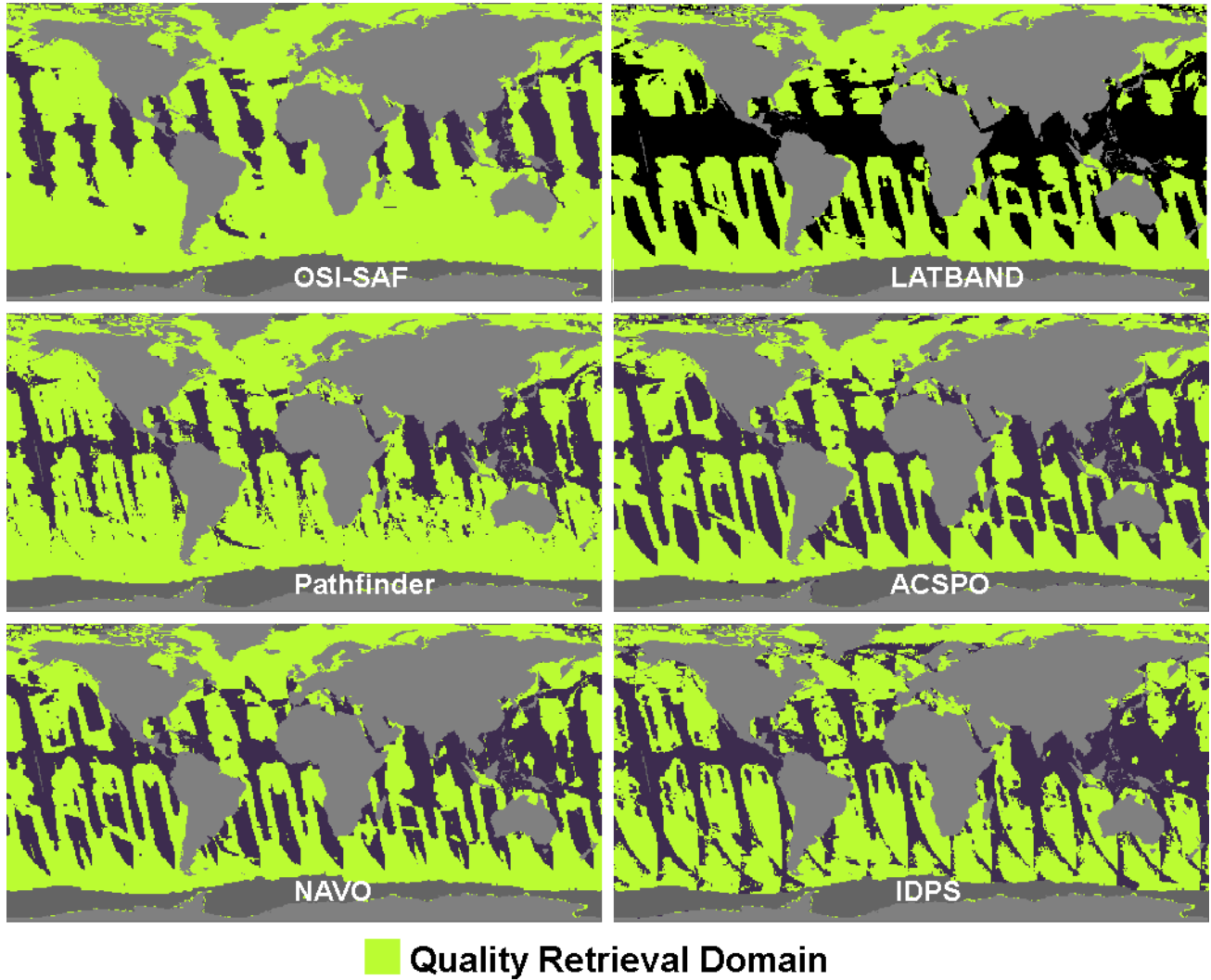


Fig. 9. Quality Retrieval Domains for six daytime algorithms, derived from maps of bias, SD and sensitivity for 24 August 2012 (Fig. 6-8), according to the following specifications: $|B| < 0.1$ K; $\sigma < 0.4$ K; $0.8 < \mu < 1.1$. The QRDs are 82.2% for OSI-SAF, 58.9% for LATBAND, 75.4% for Pathfinder, 67.2% for ACSPO, 62.8% for NAVO, and 60.4% for IDPS.

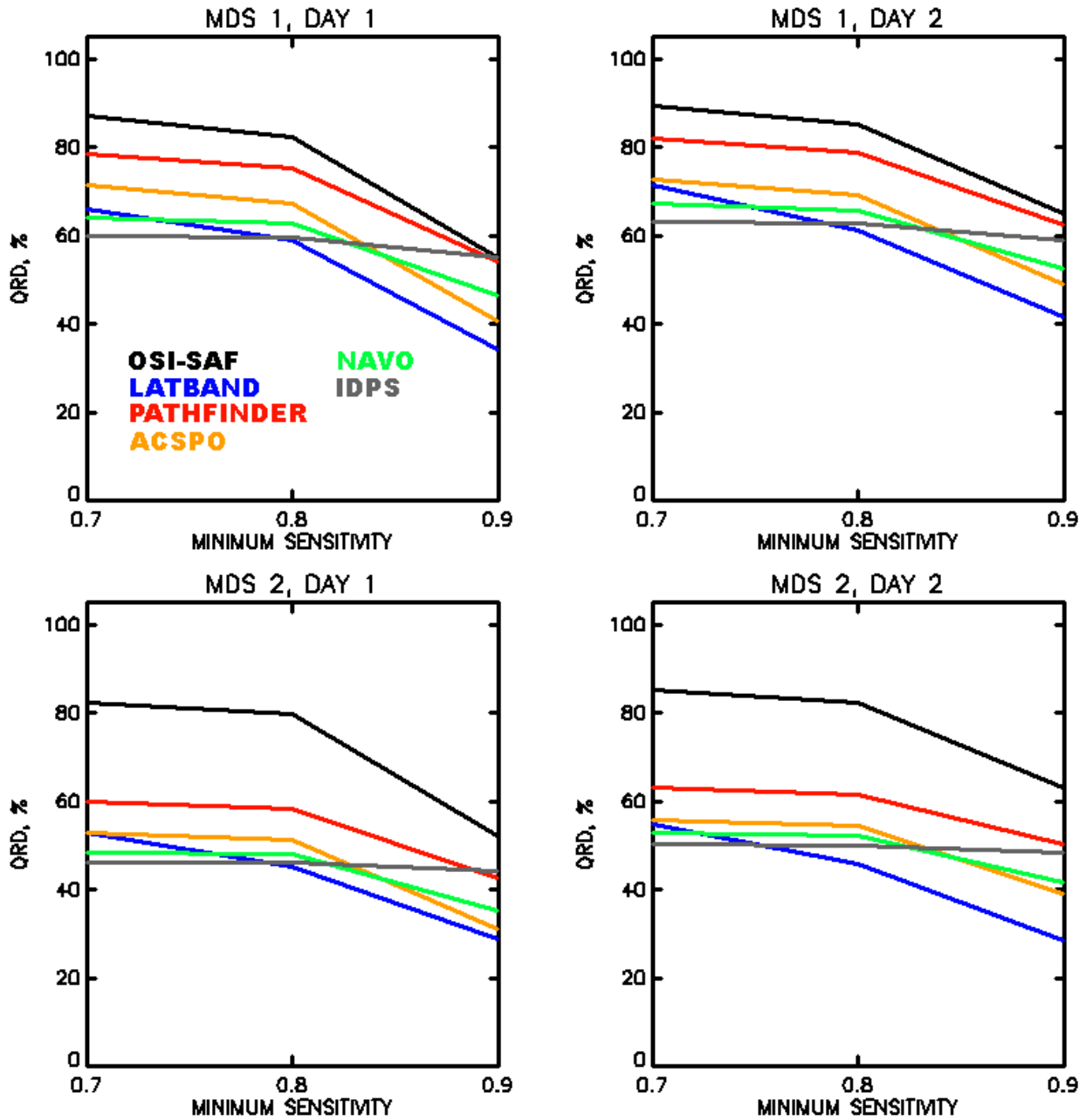


Fig. 10. QRD as a function of specification on minimum sensitivity with the following fixed specifications on bias and SD: $|B| < 0.1$ K, $\sigma < 0.4$ K, for six daytime SST algorithms, for four combinations of two MDS and two days of VIIRS observations..

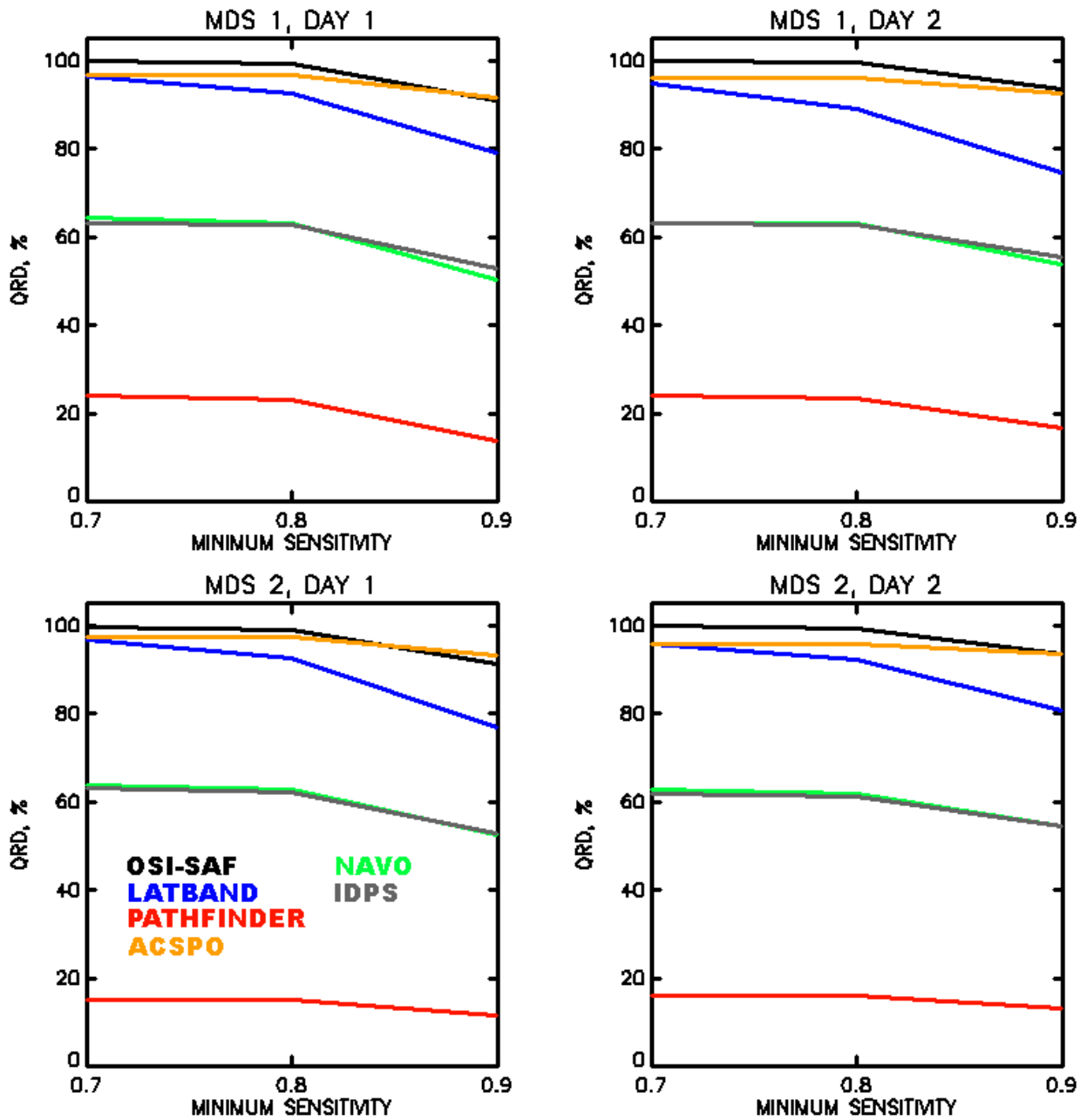


Fig. 11. QRD as a function of specification on minimum sensitivity with the following fixed specifications on bias and SD: $|B| < 0.1$ K, $\sigma < 0.4$ K, for six nighttime SST algorithms, for four combinations of two MDS and two days of VIIRS observations..

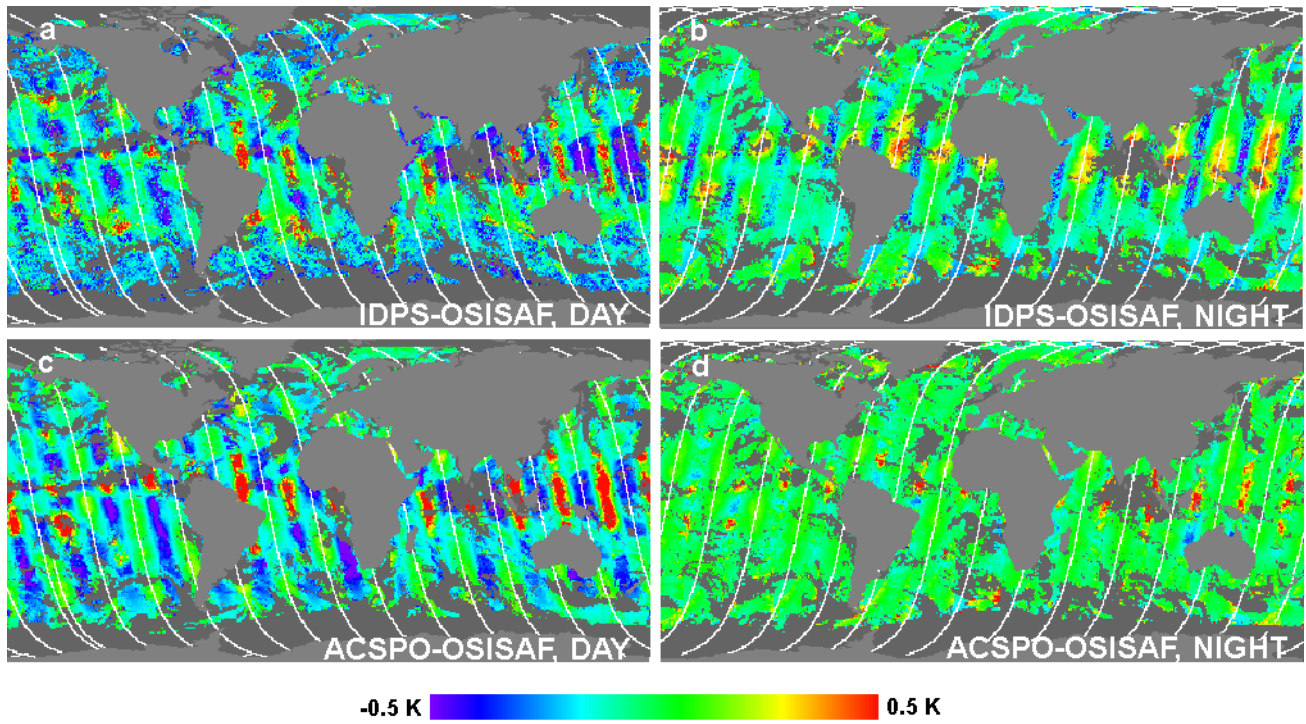


Fig. 12. The maps of the (left panels) daytime and (right panels) nighttime difference between SST retrieved from VIIRS data with (top panels) IDPS and OSI-SAF algorithms and (bottom panels) ACSPO and OSI-SAF algorithms on 29 October 2012. The white curves show centers of the swaths.

798

799

TABLES

800

801

802 Table 1. List of acronyms.

ACSPO	Advanced Clear-Sky Processor for Oceans
ACSM	ACSPO Clear-Sky Mask
AVHRR	Advanced Very High Resolution Radiometer
AWG	GOES-R Algorithm Working Group
BT	Brightness Temperature
CRTM	Community Radiative Transfer Model
DSST	AVHRR-based 0.25° Daily High-Resolution Blended SST analysis
DPA	JPSS Data Products and Algorithms Team
GFS	Global Forecast System
GOES-R	Geostationary Operational Environmental Satellite - R
IDPS	Interface Data Processing Segment
iQuam	In situ SST Quality Monitor
JDE	JPSS Data Exploitation
JPSS	Joint Polar Satellite System
LUT	Look-up Table
MCSST	Multichannel SST
MDS	Dataset of Matchups
MICROS	Monitoring of IR Clear-sky Radiances over Oceans for SST
MODIS	Moderate Resolution Imaging Spectroradiometer
NAVO	Naval Oceanographic Office
NCEP	National Center for Environmental Prediction

NDE	NOAA Data Exploitation program
NGAS	Northrop Grumman Aerospace Systems
NOAA	National Oceanic and Atmospheric Administration
NODC	National Oceanographic Data Center
NLSST	Nonlinear SST
NPOESS	National Polar-orbiting Environmental Satellite System
NRL	Naval Research Laboratory
OSPO	Office of Satellite Products and Operations
OSTIA	Operational SST and Sea Ice Analysis
QRD	Quality Retrieval Domain
OSI-SAF	EUMETSAT Ocean and Sea Ice Satellite Application Facility
RTM	Radiative Transfer Model
SD	Standard deviation
SQUAM	SST Quality Monitor
SNPP	Suomi National Polar-orbiting Partnership satellite
SST	sea surface temperature
STAR	NOAA Center for Satellite Applications and Research
STPW	“Slant” total precipitable water vapor content along line of sight
TPW	Total precipitable column water vapor content in the atmosphere
VIIRS	Visible Infrared Imager Radiometer Suite
VCM	VIIRS Cloud Mask
VZA	Satellite View Zenith Angle

803

804

805 Table 2. Daytime statistics of retrieved SST minus in situ SST, averaged over 10 months MDS.

Statistics	NRL	OSI-SAF	LATBAND	Pathfinder	NAVO	ACSPO	IDPS
Bias	0.0 K	0.016 K	0.006 K	0.005 K	0.0 K	0.0 K	-0.002 K
SD	0.362 K	0.424 K	0.445 K	0.448 K	0.463 K	0.466 K	0.476 K

806

807

Table 3. The Quality Retrieval Domain estimated for six daytime algorithms, using various

specifications on bias, SD, and sensitivity to true SST (μ). Maximum values of QRD for every set of

specifications are shown in bold.

Bias spec	SD spec	OSI-SAF	LATBAND	Pathfinder	ACSPO	NAVO	IDPS
$0.9 < \mu < 1.1$							
0.2 K	0.4 K	54.9%	43.7%	55.3%	50.7%	59.3%	58.4%
	0.5 K	55.0%	44.4%	57.1%	51.5%	61.3%	64.1%
	0.6 K	55.0%	44.4%	57.3%	51.5%	61.4%	64.3%
0.1 K	0.4 K	54.9%	34.4%	54.2%	40.5%	46.5%	55.7%
	0.5 K	55%	34.6%	55.3%	40.9%	46.9%	60.8%
	0.6 K	55%	34.6%	55.5%	40.9%	46.9%	61.0%
$0.8 < \mu < 1.1$							
0.2 K	0.4 K	82.2%	70.2%	78.8%	79.5%	79.5%	63.7%
	0.5 K	82.6%	72.6%	83.3%	83.4%	85.2%	77.7%
	0.6 K	82.6%	72.6%	83.8%	83.6%	85.5%	79.4%
0.1 K	0.4 K	82.2%	58.9%	75.4%	67.2%	62.8%	60.4%
	0.5 K	82.6%	60.0%	78.7%	69.6%	65.8%	69.9%
	0.6 K	82.6%	60.0%	79.1%	69.8%	66.1%	71.6%
$0.7 < \mu < 1.1$							
0.2 K	0.4 K	87.2%	77.7%	82.6%	83.2%	81.9%	64.1%
	0.5 K	92.1%	83.2%	92%	92.9%	93.1%	81.7%
	0.6 K	92.2%	83.6%	93.8%	94.7%	95.4%	86.5%
0.1 K	0.4 K	87.2%	65.9%	78.6%	71.3%	64.4%	60.7%
	0.5 K	92.1%	69.7%	86.5%	78.8%	72.8%	72.2%
	0.6 K	92.2%	70.1%	88%	79.8%	74.3%	76.9%

813 Table 4. Nighttime statistics of retrieved SST minus in situ SST, averaged over 10 months MDS.

Statistics	OSI-SAF	LATBAND	ACSPO	NAVO	IDPS	Pathfinder
Bias	0.0 K	0.006 K	0.0 K	0.0 K	0.0 K	0.004 K
SD	0.350 K	0.355 K	0.359 K	0.381 K	0.382 K	0.538 K

814

815

816

Table 5. The Quality Retrieval Domain estimated for six nighttime algorithms, using different specifications on bias, SD sensitivity to true SST (μ). Maximum values of QRD for every set of specifications are shown in bold.

Bias spec	SD spec	OSI-SAF	ACSPO	LATBAND	NAVO	IDPS	Pathfinder
$0.9 < \mu < 1.1$							
0.2 K	0.4 K	90.8%	94.9%	81.6%	78.7%	82.7%	25.5%
	0.5 K	90.8%	94.9%	81.6%	78.8%	82.7%	52.3%
	0.6 K	90.8%	94.9%	81.6%	78.8%	82.7%	53.5%
0.1 K	0.4 K	90.8%	90.6%	78.3%	50.3%	53.4%	14.4%
	0.5 K	90.8%	90.6%	78.3%	50.3%	53.4%	40.9%
	0.6 K	90.8%	90.6%	78.3%	50.3%	53.4%	41.5%
$0.8 < \mu < 1.1$							
0.2 K	0.4 K	99.1%	100%	95.5%	93.1%	94.4%	44.5%
	0.5 K	99.1%	100%	95.5%	93.2%	94.6%	78%
	0.6 K	99.1%	100%	95.5%	93.2%	94.6%	80.5%
0.1 K	0.4 K	99.1%	95.7%	92.2%	63.1%	63.6%	23.5%
	0.5 K	99.1%	95.7%	92.2%	63.1%	63.6%	55.8%
	0.6 K	99.1%	95.7%	92.2%	63.1%	63.6%	57.5%
$0.7 < \mu < 1.1$							
0.2 K	0.4 K	100%	100%	99.4%	96.2%	97.8%	46.0%
	0.5 K	100%	100%	99.4%	96.2%	97.8%	84.4%
	0.6 K	100%	100%	99.4%	94.7%	97.8%	90.8%
0.1 K	0.4 K	100%	95.7%	96.1%	64.2%	64.4%	24.4%
	0.5 K	100%	95.7%	96.1%	64.2%	64.4%	60.7%
	0.6 K	100%	95.7%	96.1%	64.2%	64.4%	65.8%

822 Table 6. Global bias, SD of VIIRS SST minus DSST and number N of “confidently clear” pixels
823 with original and new (OSI-SAF) SST algorithms for IDPS and ACSPO.

Processing system	Original algorithm			OSI-SAF algorithm		
	Bias	SD	N	Bias	SD	N
Day						
IDPS	0.16 K	0.87 K	113018840	0.32 K	0.79 K	113019830
ACSPO	0.42 K	0.62 K	114212320	0.31 K	0.58 K	117085932
Night						
IDPS	-0.05 K	0.64 K	117700852	-0.02 K	0.61 K	117700793
ACSPO	0.10 K	0.45 K	104371534	-0.09 K	0.44 K	104786847

824

825